Remapping and realignment in the human hippocampal formation predict context-dependent spatial behavior

Joshua B. Julian[1,2*] & Christian F. Doeller[1,3*]

(1) Kavli Institute for Systems Neuroscience, Centre for Neural Computation, The Egil and Pauline Braathen and Fred Kavli Centre for Cortical Microcircuits, Norwegian University of Science and Technology, Trondheim, Norway; (2) Present address: Princeton Neuroscience Institute, Princeton University, Princeton, NJ, USA; (3) Max Planck Institute for Human Cognitive and Brain Sciences, Leipzig, Germany.

*****Correspondence: joshua.b.julian@gmail.com or doeller@cbs.mpg.de

ABSTRACT

To guide spatial behavior, the brain must retrieve memories that are appropriately associated with different navigational contexts. Contextual memory may be mediated by cell ensembles in the hippocampal formation that alter their responses to changes in context, processes known as remapping and realignment in the hippocampus and entorhinal cortex, respectively. However, whether remapping and realignment guide context-dependent spatial behavior is unclear. To address this issue, human participants learned object-location associations within two distinct virtual-reality environments and subsequently had their memory tested during fMRI scanning. Entorhinal grid-like representations showed realignment between the two contexts, and coincident changes in fMRI activity patterns consistent with remapping were observed in the hippocampus. Critically, in a third ambiguous context, trial-by-trial remapping and realignment in the hippocampal-entorhinal network predicted context-dependent behavior. These results reveal the hippocampal-entorhinal mechanisms mediating human contextual memory and suggest that the hippocampal formation plays a key role in spatial behavior under uncertainty.

INTRODUCTION

Successful spatial behavior requires the ability to separate memories based on the environmental context experienced at encoding: “in which room did I leave my keys?”; “is that good restaurant in SoHo or Brooklyn?”; “do I turn left in the park or on the street?” Examples of this contextual memory process are ubiquitous, and impairment of this process is a hallmark of disorders such as Alzheimer’s disease[1], where patients often fail to appropriately recall the navigational context experienced at encoding, thus impairing their overall navigation abilities.

How does the human brain retrieve contextual memories to guide spatial behavior? Lesion and patient studies have demonstrated that the hippocampus and entorhinal cortex are necessary for context-dependent behavior[1,2], and contextual memory is a foundational component of many long-standing theories of hippocampal function[3–11]. If the hippocampal formation mediates contextual memory, as such theories presuppose, then changes in context representations in the hippocampal formation should be related to detectable changes in behavior during spatial memory tasks. Despite decades of research on the role of the hippocampal formation in contextual memory, no previous studies have interrogated context-specific signals in the human hippocampal-entorhinal network during the execution of a spatial memory task that unambiguously dissociates contextual memory from nonmnemonic factors.

Spatial context may be represented in the hippocampus through the activity of place cells that fire whenever a navigator occupies particular environmental locations[12]. Different place cells fire in different locations, and thus as a population are thought to represent a cognitive map of the local spatial context[8]. When context is altered, place cells undergo a process known as remapping, in which all place cells shift their relative firing fields to new locations or stop firing altogether, thereby forming decorrelated representations of distinct environments[13,14]. Functional MRI (fMRI) studies have likewise found that hippocampal activity patterns reliably change across distinct virtual-reality environments, akin to population-level “remapping”[15–17]. Remapping may be driven by entorhinal inputs to the hippocampus[18–20]. The entorhinal cortex contains several types of place-modulated neurons, including grid cells that fire whenever a navigator occupies a hexagonal lattice of environmental locations[21]. An fMRI signature of grid cell activity is observed in human entorhinal cortex during virtual-reality navigation[22]. Across different contexts, coincident with place cell remapping, grid cells coherently shift and rotate their firing fields, a process known as grid realignment[20,23]. Despite being induced by changes in spatial context, whether hippocampal remapping and/or grid realignment mediate contextual memory is unclear[3,24].

To investigate the link between hippocampal-entorhinal context representations and contextual memory, we related fMRI proxies of remapping and realignment in humans to context-dependent spatial memory during virtual-reality navigation. We trained human participants (n=24) to learn the locations of four target objects in two distinct virtual-reality (VR) arenas. On each trial, participants saw a word denoting one of the target objects, were teleported into one of the arenas, and then indicated the target object’s location for that trial by navigating to it from a random start location and making a button-press response (the ‘‘recall” phase; Figure 1a). Participants were then teleported to a new random position in the same

arena and the target object for that trial appeared in its correct location and was collected (the ‘‘feedback’’ phase). One arena was limited by a square boundary wall (“Square”) and the other was limited by a circular boundary wall (“Circle”) (Figure 1b). Each arena was also surrounded by four unique distal cues that could be used for orientation. The identities of the target objects were the same for both the Circle and Square. Therefore, to learn the target object locations in each arena, participants needed to learn the appropriate location-context associations through the feedback provided (Extended Data Figure 1).

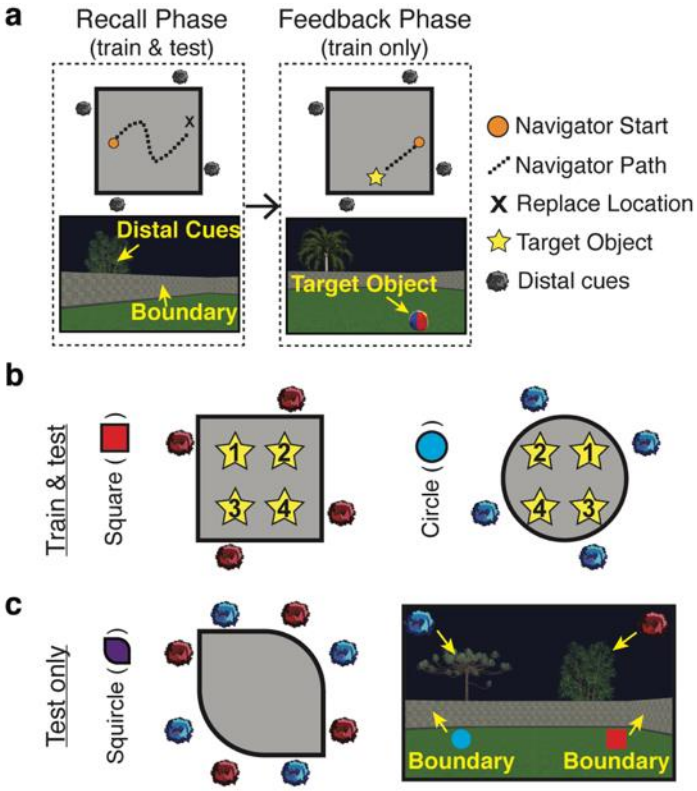

Figure 1. Context-dependent spatial memory task. a, Trial structure (after initial learning of object locations; see Methods). On each trial, participants navigated to the remembered location of the target object (‘‘recall’’ phase) and, after a 2s delay with a black screen, received feedback (‘‘feedback’’ phase). The top shows a map of the virtual trajectory taken by the participant on each phase of a typical trial, and the bottom shows example views of the virtual environment from the participant’s perspective. The name of the target object for each trial was shown in the center of a black screen prior to the start of the recall phase. **b,** Participants learned four object locations in two arenas (“Square”, “Circle”) over four blocks of training trials per arena. Object identities were the same for both arenas, but each of the four objects occupied a different relative location across arenas. Following training, object location memory was tested in these two arenas using the recall phase only. Unlike training, participants were teleported into a random arena at the start of each trial during testing (with the constraint that the same arena could not be tested on more than two consecutive trials). **c**, Memory for object locations was also tested in a third half-square half-circular arena (“Squircle”). Left: schematic of the Squircle. Right: example view of the Squircle from the participant’s perspective.

Following behavioral training outside of the MRI scanner, participants underwent fMRI scanning while performing the same object location memory task. Unlike training, participants did not receive feedback after each trial during scanning (i.e., they performed the recall phase only). At the start of each trial during testing, participants had their view rotated automatically around 360º once (12s duration) to encourage them to identify their current context before they began the recall phase. In addition to the Square and Circle (40% of trials per context), memory for object locations during scanning was also tested in a third ambiguous half-square half-circle

arena (“Squircle” arena; 20% of trials) (Figure 1c). The Squircle was surrounded by eight distal orientational cues, four from the Square and four from the Circle. Participants were not informed about the Squircle manipulation in advance and were instructed to indicate the object’s location wherever they saw fit if they were uncertain about the correct object location.

The ambiguous Squircle provides a means of assessing the relationship between hippocampal-entorhinal context representations and memory-guided spatial behavior. In particular, for each target object, there are two possible “correct” locations in the Squircle, one more consistent with the location in the Circle, and one more consistent with the location in the Square. Thus, to recall object locations in the Squircle, on each Squircle trial participants needed to retrieve either a Square- or Circle-consistent contextual memory. If the hippocampal-entorhinal network mediates contextual memory, we hypothesized that hippocampal-entorhinal signals would be predictive of which contextual memory is retrieved in the Squircle on a trial-by-trial basis.

RESULTS

Spatial behavior in the ambiguous Squircle context reflects contextual memory

All participants reported noticing the Squircle manipulation during debriefing following the experiment. Due to ambiguity in target object locations in the Squircle, participants exhibited longer response latencies in the Squircle than both the Square and Circle (Figure 2a). These longer response latencies were primarily due to greater time spent stationary without VR-walking in the Squircle relative to the two training contexts, as VR-walking path tortuosity was similar in all contexts (Figure 2b). For each Squircle trial, to assess the similarity of spatial memory retrieval to the Square and Circle, we computed the distance between each recalled object’s location in the Squircle and that object’s corresponding location in the Square and in the Circle. Participants tended to recall target objects in the Squircle in either the Square- or Circle-consistent location but rarely elsewhere (Figure 2c), and at similar distances from the closest context-consistent locations as they did from the correct locations in the Square and Circle (Figure 2d). Accordingly, the recalled target object locations in the Squircle were closer to context-consistent locations than would be expected by random chance, both overall (4.6±0.42vm from a context-consistent location vs. 10.2vm by random chance; t_{23}=20.12, *CI*=[5.06-6.22], p=2.11x10^{-16}) and in each participant (Kolmogorov–Smirnov tests, α=0.05; Figure 2e). Across participants, the distance of recalled locations in the Squircle to the closest context-consistent location strongly correlated with the average distance of recalled locations from the correct locations in the Square and Circle (Figure 2f), even after controlling for response latency and path tortuosity in the Square and Circle (partial correlation, r=0.78, p=1.58x10^{-5}), suggesting that deviations from context consistency in the Squircle may have been driven by spatial memory precision in the Square and Circle and not domain general factors.

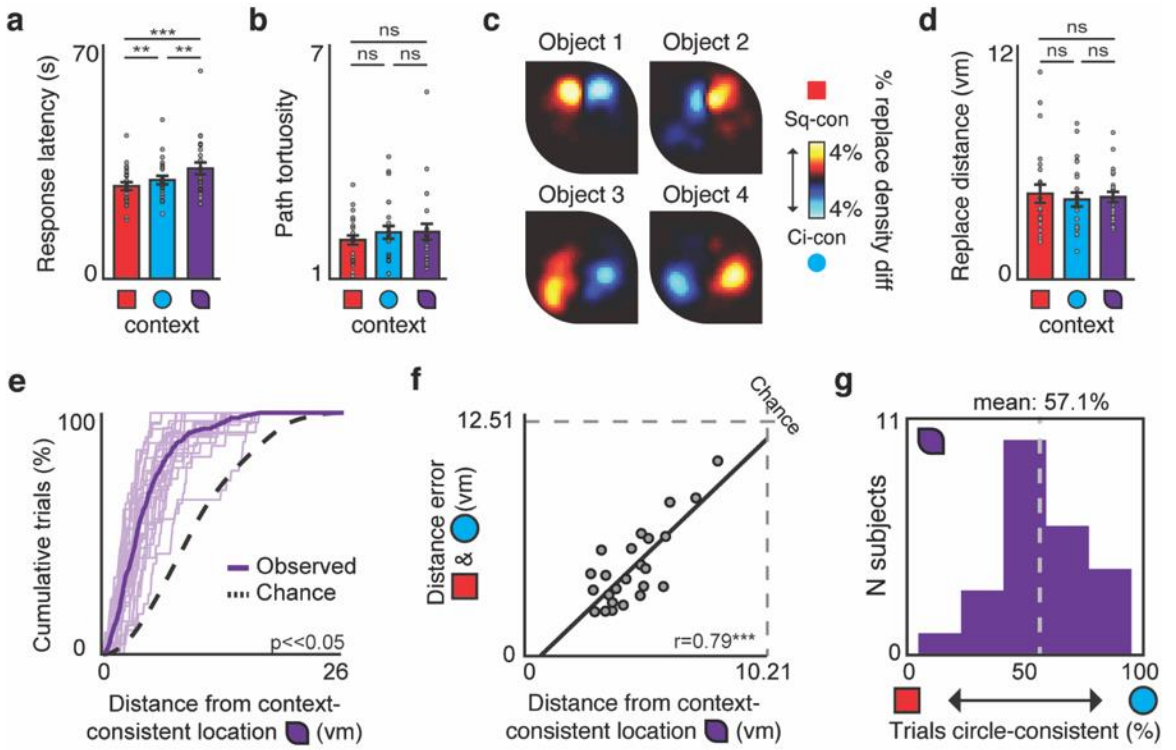

Figure 2. Contextual memory retrieval in the ambiguous Squircle context. **a,** Response latencies (length of recall phase) during testing in the Square (Sq), Circle (Ci), and Squircle (t-tests, two tailed; Squircle vs. Sq: t_{23}=4.19, *CI*=[2.85-8.43], p=0.0004; Squircle vs. Ci: t_{23}=3.05, *CI*=[1.19-6.20], p=0.006; Sq vs. Ci: t_{23}=3.44, *CI*=[0.77-3.12], p=0.002). **b,** Path tortuosity in the Sq, Ci, and Squircle during testing (one-way rmANOVA, $F_{2,46}$=1.10, p=0.342). Tortuosity was computed as the observed path length divided by the length of the shortest possible path between each trial's starting location and the recalled location. **c,** Heat maps depicting the difference in Sq- and Ci-consistent recalled locations (% Sq-con - % Ci-con trials) in the Squircle, separately for each of the four target objects (see Methods). **d,** Distance of recalled locations during testing from the correct location in Sq and Ci, and from the nearest context-consistent location in the Squircle (one-way rmANOVA, $F_{2,46}$=0.51, p=0.606). **e,** Cumulative distribution functions of recalled location distances from the nearest context-consistent location across all Squircle trials for each participant (light purple) and on average (dark purple), compared to the distribution of distances from the nearest context-consistent locations expected from random behavior (Chance). **f,** Across participants, the average distance of recalled locations from the nearest context-consistent location in the Squircle correlated with the average distance of recalled locations from the correct locations (distance error) in the Sq and Ci (p=4.51x10^{-6}, two-tailed). Dotted lines denote error expected by chance. Chance error is lower in the Squircle than Sq/Ci because each target object had two possible context-consistent locations in the Squircle (one Sq-con, one Ci-con). **g,** Histogram of the percentage (%) of total Squircle trials during which participants recalled target objects in Ci-con locations (compared to 50% no-bias baseline: sign-test, p=0.15, two-tailed). Throughout the figure, error bars indicate ±1 SEM; dots denote individual participants (n=24); **p<0.01, ***p<0.001

Since participants tended to recall target objects in the Squircle as being in either the Square or Circle-consistent locations, but not elsewhere, we classified each Squircle trial as being either Square-consistent or Circle-consistent based on the distance between the recalled target object location and the closest context-consistent location (i.e., based on whichever training context had a relatively closer location to the recalled location for each target object). Across participants, there was no overall bias to recall objects more often in either Square- or Circle-consistent locations (Figure 2g). Across trials, each participant recalled target objects in both Square- and Circle-consistent locations. Follow-up analyses reported in Extended Data Figure 2 found that, other than the recalled target object locations, behavior was quantitatively indistinguishable between Square- and Circle-consistent Squircle trials. Further, as detailed in Extended Data Figure 3, recalled locations in the Squircle were *not* predicted by the relative strength of object-location associations learned during training, or a participant's trial history over the course of testing, or

each Squircle trial's starting location. Participants also did not use a strategy of replacing target objects in the Squircle at the location intermediate between the two context-consistent locations. However, contextual memory retrieval in the Squircle was not random; for each target object, each participant tended to have a unique contextual preference for that object. Together, these observations suggest that spatial behavior in the Squircle was guided by the retrieval of Square and Circle contextual memories.

Hippocampal remapping distinguishes between contexts

As a prerequisite for examining the relationship between hippocampal context representations and contextual memory in the Squircle, we first needed to establish the existence of an fMRI proxy for hippocampal remapping between the Circle and Square. To do so, we trained a correlation-based nearest-neighbor multivariate pattern classification algorithm to distinguish between the Square and Circle contexts (see Methods), akin to population vector analyses of place cell remapping[14]. We estimated the average bilateral hippocampal activity patterns associated with the Square and with the Circle during the recall phase separately for each scan run. Leave-one-run-out cross-validated context classification accuracy from the hippocampus was significantly higher than expected by chance (71.0% versus 50.0% in the permutation test, t_{23}=9.90, *CI*=[0.17-0.25], p=9.24x10^{-10}; t_{23}=9.67, *CI*=[0.17-0.26], p=7.21x10^{-10} versus 50% theoretical chance baseline; Extended Data Figure 4), indicating that hippocampal activity patterns reliably differed between the Square and Circle on average. We next applied the same classifier to activity patterns elicited during *single trials* within each held-out run. Context classification accuracy from the hippocampus was still significantly higher than expected by chance (55.6% versus 49.9% in the permutation test, t_{23}=4.95, *CI*=[0.03-0.08], p=5.24x10^{-5}; t_{23}=4.82, *CI*=[0.03-0.08], p=7.24x10^{-5} compared to 50% theoretical chance baseline; Figure 3a). There were thus reliably different hippocampal activation patterns elicited in the Square and Circle on a trial-by-trial basis.

We subsequently examined the evolution of hippocampal context representations during Square and Circle trials. For each volume of fMRI data, we computed a Contextual Similarity (CS) Score as the difference in multivariate pattern similarity (Fisher-transformed Pearson correlation coefficient) between each volume's hippocampal activation pattern and the average across-run Square and Circle activity patterns. CS Scores thus correspond to the extent to which hippocampal activity patterns were more like those elicited in the Square or the Circle across scan runs. Since the recall phase was self-paced, trials were of variable lengths. To average the volume-by-volume CS Scores across different trials, each recall phase was resampled to 30 timepoints, such that the start and end of each resampled recall phase corresponded to the actual start (offset by 6.12s to account for the hemodynamic lag) and end of each trial's recall phase. Over the course of the recall phase, hippocampal activity patterns were on average more similar to those elicited in same context across scan runs than the opposite context (Figure 3b). These results are consistent with the existence of reliable remapping of hippocampal context representations.

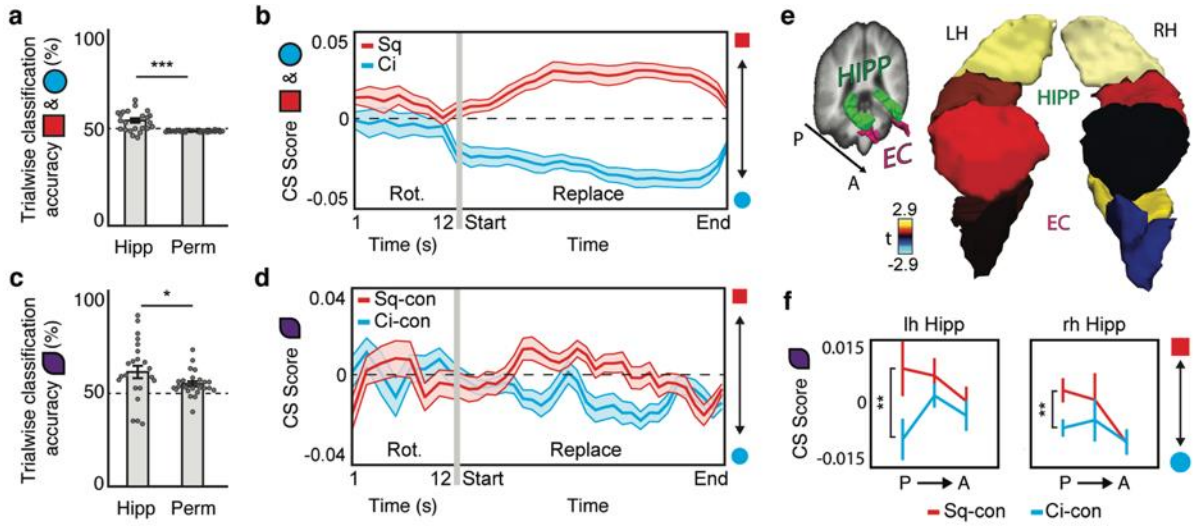

Figure 3. Hippocampal remapping distinguishes between contexts and predicts memory-guided behavior. a, Trial-wise hippocampal (Hipp) context classification accuracy for Square (Sq) and Circle (Ci) trials was significantly higher than in a permutation test (Perm) (t-test). The dotted line indicates theoretical chance baseline (50%). Note that independent voxel selection limited each participant's Hipp mask to only contextually-modulated voxels (Methods; Supplementary Figures 1-2). **b,** Contextual similarity of hippocampal activity (CS Score = z_{square} - z_{circle}) over time, separately for Sq (red) and Ci (blue) trials (average Sq vs Ci recall phase: t_{23}=12.32, *CI*=[0.04-0.06], p=6.53x10^{-12}). Rot corresponds to the pre-trial rotation period during which the participant's VR-facing direction was automatically rotated 360° prior to the recall phase start. CS scores >0 (<0) indicate that an activation pattern is more similar to that elicited in the Square (Circle) across scan runs. **c,** Trial-wise Hipp Sq- vs Ci-consistent Squircle contextual memory classification accuracy was significantly higher than in a permutation test (t-test). Classification accuracy did not differ between the Squircle and Sq/Ci (t_{23}=0.33, p=0.746, two-tailed, controlling for Perm baseline differences). **d,** Hipp CS Scores over time during Sq-con (red) and Ci-con (blue) Squircle trials (average Sq-con vs. Ci-con recall phase: t_{23}=1.75, *CI*=[-0.002-0.02], p=0.047). **e,** Average Hipp CS Scores during the recall phase of Sq- vs. Ci-con Squircle trials in three Hipp subregions (anterior, middle, posterior; Supplementary Figure 1) in each hemisphere, computed without voxel selection. CS scores differed (n=24; t-test) in right posterior Hipp (p=0.005, p_{FWE}=0.030) and marginally in left posterior Hipp (p=0.009, p_{FWE}=0.053), but not elsewhere (p_{FWE}>0.05). In a complementary exploratory analysis of entorhinal cortex (EC), EC was divided into two subregions (posterior, anterior) in each hemisphere. CS scores differed only in the posterior right EC (p=0.038) but did not survive FWE-correction. **f,** Hipp CS scores during the recall phase of Sq-con and Ci-con Squircle trials for the six HIPP subregions depicted in Figure 3e. Throughout the figure, error bars or error bands indicate ±1 SEM; dots denote individual participants (n=24); ^{ns}p>0.05, *p<0.05, **p<0.01, ***p<0.001.

Hippocampal remapping predicts contextual memory in the ambiguous Squircle context

We next tested the relationship between hippocampal remapping and contextual memory in the Squircle. The contextual memory retrieved during each Squircle trial was classified as being Square- or Circle-consistent based on participant behavior as previously described. We then applied the same classification algorithm trained to distinguish between the Square and Circle contexts to each Squircle trial's hippocampal activity pattern. Trial-by-trial Squircle contextual memory classification accuracy was significantly higher than expected by chance (58.8% versus 52.5% in the permutation test, t_{23}=2.45, *CI*=[0.01-0.12], p=0.011; t_{23}=2.95, *CI*=[0.03-0.15], p=0.004 compared to 50% theoretical chance baseline; Figure 3c). We also computed the CS Score for each volume of fMRI data, separately for Square- and Circle-consistent Squircle trials. Over the course of the recall phase, hippocampal activity patterns were on average more similar to those elicited in the context consistent with memory than with the inconsistent context (Figure 3d). Repeating the same analysis for three distinct hippocampal subregions (posterior, middle, anterior), separately for each hemisphere, we observed that activity patterns in the Squircle

were most strongly consistent with contextual memory in the right posterior hippocampus (Figure 3e-f). Together, these results suggest that trial-by-trial hippocampal remapping supports contextual memory.

Sensitivity and tolerance of hippocampal context representations to nonmnemonic factors

If hippocampal activity patterns elicited in the Squircle exclusively reflect contextual memory, we would expect such activity patterns to be tolerant to changes in nonmnemonic factors, including VR-locomotory behavior, location, visual input, and target object identity. We tested hippocampal sensitivity to each of these nonmnemonic factors in turn.

To test whether hippocampal context representations were tolerant to changes in VR-locomotory behavior, CS Scores were computed separately for VR-walking and VR-stationary epochs during the recall phase. Unexpectedly, unlike in the Square and Circle (Figure 4a), Squircle CS Scores strongly differed between Square- and Circle-consistent trials when participants were VR-walking, but not when they were VR-stationary (Figure 4b; see also Extended Data Figure 5 for behavioral control analyses). We will return to the source of dissociation between contextual memory and hippocampal activity during VR-stationary epochs below. Importantly, during VR-walking epochs, hippocampal context representations were tolerant to changes in the navigator's VR-walking location within the Squircle (Figure 4c). This last observation rules out the possibility that context representations were an artifact of hippocampal coding of proximal boundary geometry (i.e., a square vs. circular corner; Figure 4d).

We next tested whether hippocampal context representations during VR-walking epochs were tolerant to changes in visual input. Squircle scenes look more similar to Square or Circle visual scenes when a participant is VR-facing more in the direction of a square or circular boundary segment, respectively. Likewise, Squircle scenes look more similar to visual scenes in the Square or Circle when a participant is VR-facing more in the direction of a distal cue present in the Square or Circle, respectively. However, during VR-walking epochs, hippocampal CS Scores were not modulated by the type of boundary segment (Figure 4e) or distal cue (Figure 4f) viewed. To further rule out whether these results were due to hippocampal coding of visual input, we also repeated the foregoing analyses for an early visual cortex (EVC) control region of interest. As detailed in Extended Data Figure 6, EVC showed a markedly different pattern during Squircle trials than the hippocampus: there was no significant difference between Square- and Circle-consistent EVC activity patterns, and CS Scores more strongly differed between Square- and Circle-consistent trials in the hippocampus than EVC, both on average during the entire recall phase (region x contextual memory rmANOVA; $F_{1,23}=4.43$, $p=0.047$, partial $\eta^2=0.161$), and especially during VR-walking epochs ($F_{1,23}=10.56$, $p=0.003$, partial $\eta^2=0.315$). Thus, hippocampal context representations are better explained by contextual memory than visual similarity.

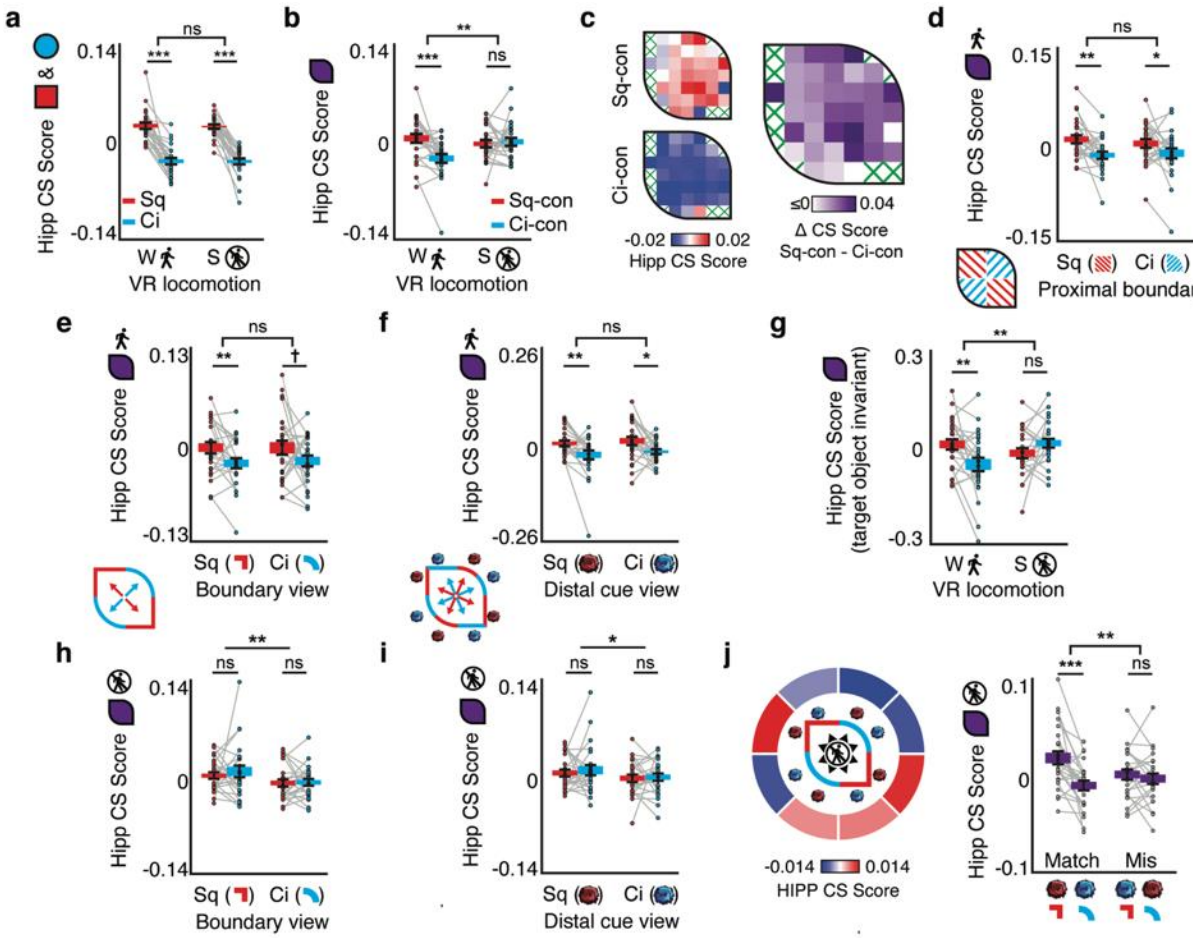

Figure 4. Hippocampal context representations in the Squircle are tolerant to changes in location and visual input, but not VR-locomotory behavior. a, Hippocampal (Hipp) Square (Sq; red) and Circle (Ci; blue) CS scores binned by VR-locomotory behavior (VR-(W)alking vs. VR-(S)tationary) (Context x VR-locomotion rmANOVA: VR-locomotion main effect, $F_{1,23}$=0.04, p=0.845; interaction, $F_{1,23}$=0.01, p=0.909). CS Scores >0 (<0) indicate that an activation pattern is more similar to that elicited in the Square (Circle) across scan runs. **b**, Hipp Sq-consistent (red; Sq-con) and Ci-consistent (blue; Ci-con) Squircle CS scores binned by VR-locomotory behavior (rmANOVA: VR-locomotion main effect, $F_{1,23}$=3.52, p=0.074; interaction, $F_{1,23}$=10.47, p=0.004, partial η^2=0.31). **c,** Hipp Squircle CS scores by VR-walking location. Left: CS scores maps during Sq-con (top) and Ci-con (bottom) trials. Right: location-wise difference between Sq-con and Ci-con CS score maps. Maps were constructed separately for each participant (resolution = 4vm^2) and then averaged across participants. Squircle locations where <2 participants VR-walked were excluded (green hatches). **d-f,** Hipp Sq-con and Ci-con Squircle CS scores during VR-walking epochs by **d,** most proximal boundary segment (Sq vs. Ci corner) (rmANOVA: proximal boundary segment main effect, $F_{1,23}$=0.17, p=0.687; interaction, $F_{1,23}$=0.86, p=0.363), **e,** boundary segment view (Sq vs. Ci corner) (rmANOVA: boundary segment view main effect, $F_{1,23}$=0.86, p=0.364; interaction, $F_{1,23}$=0.76, p=0.392), **f,** distal cue view (Sq vs. Ci distal cue) (rmANOVA: distal cue view main effect, $F_{1,23}$=0.91, p=0.350; interaction, $F_{1,23}$=0.02, p=0.901). **g**, Hipp Sq-con and Ci-con Squircle CS scores recomputed using a target-object-invariant context classifier, binned by VR-locomotory behavior (rmANOVA: contextual memory main effect $F_{1,23}$=1.07, p=0.313, VR-locomotion main effect, $F_{1,23}$=1.58, p=0.222; interaction, $F_{1,23}$=12.16, p=0.002, partial η^2=0.53). CS Scores differed between Sq- and Ci-con trials during VR-walking (t_{23}=2.87, *CI*=[0.02-0.11], p=0.004), but not VR-stationary epochs (t_{23}=-1.69, p=0.947). **h-i**, Hipp CS scores during VR-stationary epochs by **h**, boundary segment view (rmANOVA: boundary segment main effect, $F_{1,23}$=10.03, p=0.004, partial η^2=0.44; interaction, $F_{1,23}$=0.38, p=0.544), **i,** distal cue view (rmANOVA: distal cue view main effect, $F_{1,23}$=6.60, p=0.017, partial η^2=0.29; interaction, $F_{1,23}$=0.10, p=0.758). **j**, Hipp CS scores during Squircle VR-stationary epochs: Left: by view direction, averaged across participants; Right: separately for boundary-segment-distal-cue combinations that matched those present in the Sq or Ci vs. mismatched (rmANOVA: match main effect, $F_{1,23}$=1.72, p=0.203; interaction, $F_{1,23}$=12.67, p=0.002, partial η^2=0.36). Throughout the figure, error bars indicate ±1 SEM; dots denote individual participants (n=24); All post-hoc t-tests 1-tailed. Uppermost significance markers denote interaction effects in panels a,b,d-g, and main effects in h-i; ^{ns}p>0.08, †p<0.08, *p<0.05, **p<0.01, ***p<0.001.

Finally, recall that for each target object, each participant tended to have a unique contextual preference for that object in the Squircle (Extended Data Figure 3). Trial-by-trial remapping of Squircle hippocampal activity patterns could thus be an artifact of coding of target object identity. To address this alternative, we separately trained four different context classifiers, each derived using all Square and Circle context trials except those from one specific target object each (see Methods). We then recomputed Squircle CS Scores by applying the particular classifier to each Squircle trial that excluded that trial's specific target object. Hippocampal activity patterns during Squircle VR-walking epochs were still more similar to those elicited in the context consistent with memory than with the inconsistent context (Figure 4g; see also Extended Data Figure 7 for Squircle contextual memory classification using this target-object-invariant context classifier). This observation rules out the possibility that trial-by-trial hippocampal remapping was induced by target object.

Why might contextual memory and hippocampal activity dissociate during Squircle VR-stationary epochs? Although participants rotated their viewing angle (i.e., they VR-turned) during both VR-walking and -stationary epochs, they VR-turned more often during VR-stationary epochs (Extended Data Figure 5c). We hypothesized that rather than focus on contextual memory during Squircle VR-stationary epochs, participants attended to the visual scene and rotated their view to accumulate visual evidence about where to indicate the target object's location. If so, we might expect hippocampal coding of visual input during VR-stationary epochs. This was indeed the case: CS Scores during VR-stationary epochs reflected the type of boundary segment (Figure 4h) or distal cue (Figure 4i) viewed, independent of contextual memory. The most robust view sensitivity was observed for viewing directions associated with Squircle scenes depicting boundary-segment-distal-cue combinations also present in the Square or Circle (Figure 4j). These results provide a potential explanation for the dissociation between hippocampal activity and contextual memory during VR-stationary epochs, as well as demonstrate that our inability to detect view sensitivity of hippocampal context representations during VR-walking epochs was not due to insufficient power to detect effects of view.

Entorhinal grid-like realignment distinguishes between contexts

Having determined that hippocampal remapping predicts context-dependent behavior during VR-walking, we next sought to examine the relationship between entorhinal grid-like realignment and contextual memory. To do so, we first needed to establish the existence of grid-like realignment between the Square and Circle contexts. We adapted a split-half analysis previously used to reveal entorhinal grid-like representations during virtual-reality navigation in single context environments[22]. In the first half of the data, we computed putative grid orientations that maximized 60° periodic grid-like fMRI signals as a function of VR-walking direction in bilateral entorhinal cortex, separately for the Square and Circle (Figure 5a). We then tested the reliability of these context-specific grid orientations in the other independent half. Grid orientations were compared across contexts relative to the common reference frame defined by the distal cues in the Squircle.

We found reliable entorhinal grid-like modulation in the Square and Circle (Figure 5b), due to grid-like signals in both the Square and Circle aligned to their respective grid orientations (Figure 5c). Yet, grid-like modulation was *not* observed in

either the Square or Circle aligned to the grid orientation from the opposite context (Figure 5c). Indeed, across participants, a greater percentage of entorhinal voxels shared a similar grid orientation across data halves within the same context than across data halves across different contexts (Figure 5d). Conducting the same split-half analysis for other non-grid rotational symmetries, we found no evidence of reliable 90° or 45° periodic signals (Extended Data Figure 8a). As a further control we repeated the same split-half analysis for EVC and for the hippocampus but observed no reliable grid-like coding in either region (Extended Data Figure 8b-c). We also detected no 60°-symmetric biases in VR-walking behavior that could explain the presence of context-specific grid-like fMRI signals (Extended Data Figure 8d). Finally, grid orientations were differentially aligned to the shape and orientation of local space in the Square and Circle, as defined by boundary geometry and the distal cues (Extended Data Figure 9), consistent with prior reports[25–28]. Together, these results provide evidence of entorhinal grid-like realignment across the Square and Circle.

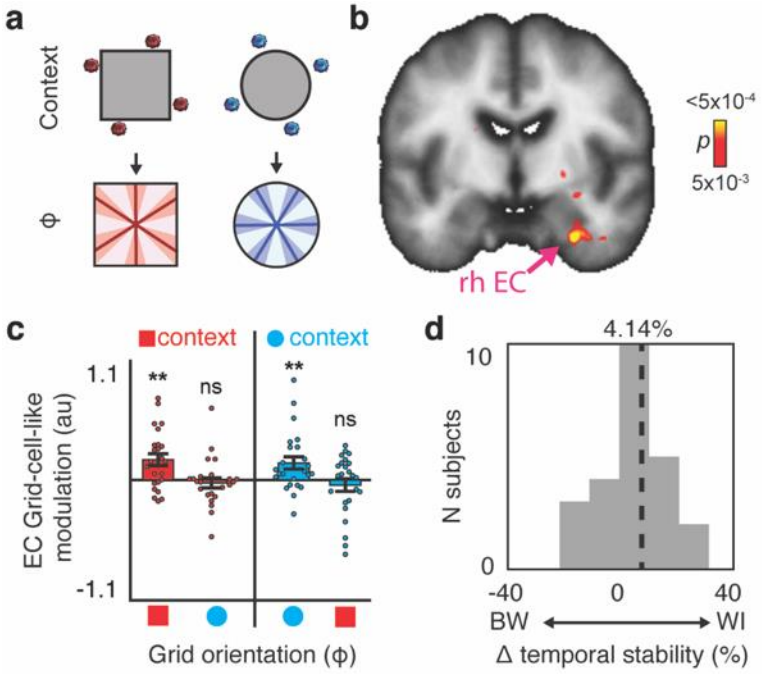

Figure 5. Entorhinal grid-like realignment distinguishes between contexts. a, Grid orientations (φ) that maximized 60° periodic grid-like fMRI signals were computed in entorhinal cortex (EC), separately for the Square (Sq) and Circle (Ci). EC grid-like modulation aligned to the context-specific φ, but not the φ of the opposite context, would be evidence of grid realignment. **b,** Reliable grid-like modulation was observed in the right EC, averaging across the Sq and Ci (t-test, peak voxel Montreal Neurological Institute coordinate: [30, -7, -34]; peak t_{23}=4.16, p_{SVC}=0.016; shown unmasked at p<0.005 for display purposes). **c,** Grid-like modulation (beta weight) in the EC subregion exhibiting grid-like modulation on average across contexts (Figure 5b; ROI defined at p<0.01) was driven by grid-like modulation in each context aligned to their respective context-specific φ (Sq: t_{23}=3.39, *CI*=[0.07-0.30], p=0.001, Ci: t_{23}=2.76, *CI*=[0.04-0.27], p=0.006; Sq versus Ci: t_{23}=0.38, p=0.708, two-tailed). No reliable grid-like modulation was found in either context aligned to the φ of the opposite context (Sq: t_{23}=-0.59, p=0.721, Ci: t_{23}=-0.82, p=0.790). **d,** Histogram of EC voxel percentage that shared a similar φ (within ±15°; temporal stability) across data halves within the same context (WI) minus the temporal stability across data halves between different contexts (BW) (n=24, sign-test, p=0.032, one-tailed). Dotted line denotes group mean. Throughout the figure, error bars indicate ±1 SEM; dots denote individual participants (n=24); ^{ns}p>0.05, *p<0.05, **p<0.01.

Entorhinal grid-like realignment predicts contextual memory in the ambiguous Squircle context

To test the relationship between grid-like realignment and contextual memory, we compared two alternative grid-like models to determine which best characterized the entorhinal fMRI signal during Squircle trials (Figure 6a). One model assumed that the grid orientation switches on a trial-by-trial basis in a manner consistent with contextual memory ("memory-consistent model"), such that the grid orientation was either the Square or Circle orientation but rotated across Squircle trials consistent with contextual memory retrieval. The other model also assumed the grid orientation switches on a trial-by-trial basis but in a manner *inconsistent* with contextual memory ("memory-inconsistent model"), such that grid-like representations had either the Square or Circle orientation when contextual memory retrieval was Circle- or Square-consistent, respectively.

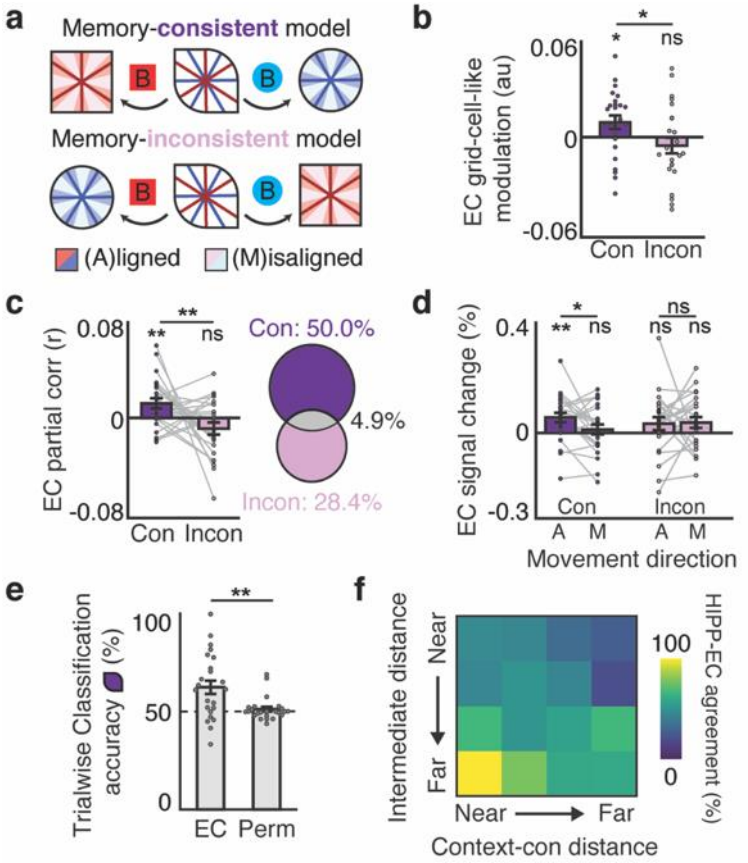

Figure 6. **Entorhinal grid-like realignment predicts memory-guided behavior. a,** Two grid-like models were fit to the bilateral entorhinal cortex (EC) fMRI signal during Squircle trials using a general linear model, one that assumed the grid orientation (φ) changed on a trial-by-trial basis consistent with contextual memory (Con; either Square or Circle φ, consistent with (B)ehavior) and the other assumed φ changed on a trial-by-trial basis inconsistent with contextual memory (Incon; either Square or Circle φ, inconsistent with B). **b,** Con and Incon grid-like modulation (beta weight) in the Squircle, averaged across all EC voxels (Con, t_{23}=2.13, CI=[0.0002-0.02], p=0.022; Incon, t_{23}=-1.06, p=0.851; Con vs. Incon, Wilcoxon Signed Rank test, p=0.023, one-tailed). **c,** Partial correlation coefficient between EC activity during Squircle trials and the activity predicted by Con or Incon, controlling for activity predicted by the alternative model. Left: Only Con yielded a significant partial correlation (Con: t_{23}=2.83, CI=[0.003-0.02], p=0.005; Incon: t_{23}=-1.75, p=0.953; Con vs. Incon: t_{23}=2.52, CI=[0.004-0.04], p=0.010, one-tailed). Right: Venn diagram depicting results of variance partitioning. Unique (non-overlapping diagram portions) and shared (overlapping portions) variances are expressed as percentages of the total variance positively explained by both models combined. Total variance explained does not sum to 100% because no variance was positively explained (shared or unique) in 4 participants (Methods). **d,** EC fMRI response (A)ligned to φ (within ±15° of a φ axis) and (M)isaligned (more than ±15° from all φ axes), separately for Con and Incon models (compared to 0 baseline: Con: A, t_{23}=3.22, CI=[0.02-0.09], p=0.004, M, t_{23}=0.72, p=0.481; Incon: A, t_{23}=1.46, p=0.157, M, t_{23}=1.95, p=0.064; A vs. M: Con, t_{23}=2.29, *CI*=[0.004-0.08], p=0.032, Incon, t_{23}=0.13, p=0.892; all two-tailed t-tests). **e,** EC Squircle contextual memory classification accuracy was significantly higher than in a permutation (Perm) test (t-test). **f,** Heatmap depicting trial-by-trial agreement (% same prediction) in decoded Squircle contextual memory between the hippocampus (Figure 3c) and EC (Figure

6e) as a function of ranked recalled distance from the location intermediate to the two possible context-con locations (D_{int}) and the nearest context-con location (D_{con}). The graph shows decreased agreement with decreasing D_{int} and increasing D_{con}. Logistic regression demonstrates that only an effect of D_{int} was reliable across the dataset (n=517 trials, χ^2=8.77, p=0.003; see Methods). Throughout the figure, error bars indicate ±1 SEM; dots denote individual participants (n=24); ^{ns}p>0.05, *p<0.05, **p<0.01.

We observed entorhinal grid-like modulation when we assumed that the grid orientation switched on a trial-by-trial basis consistent with contextual memory, but not inconsistent (Figure 6b). Similar results were obtained in a variance partitioning analysis that tested the unique contribution of each grid-like model to entorhinal activity (Figure 6c). Memory-consistent grid-like modulation was driven by greater fMRI activation when VR-walking was aligned than misaligned with the three memory-consistent grid axes; by contrast, there was no significant difference in activation between VR-walking directions aligned or misaligned to memory-inconsistent grid axes (Figure 6d). Control analyses confirmed that these results could not be explained by the presence of a single fixed grid orientation across all Squircle trials, or by a difference in 60°-symmetric VR-walking behavior between Square- and Circle-consistent Squircle trials (Extended Data Figure 10).

To verify that grid orientations indeed realigned on a trial-by-trial basis in the Squircle consistent with contextual memory, we generated two grid-like predictions for entorhinal activity during each Squircle trial, one with the Square grid orientation and the other with the Circle grid orientation. For each participant, contextual memory was then predicted for each Squircle trial based on whichever of the two predictors was more similar to entorhinal activity (Spearman rank correlation coefficient) during that trial. Squircle contextual memory classification accuracy was significantly higher than expected by chance (62.7% versus 51.6% in a permutation test, t_{23}=3.42, *CI*=[0.04-0.18], p=0.001; t_{23}=3.68, *CI*=[0.06-0.20], p=0.0006 compared to 50% theoretical chance baseline; Figure 6e). Notably, across all Squircle trials, when grid realignment and hippocampal remapping predicted retrieval of *different* contextual memories, participants recalled target object locations as closer to the location intermediate between the two possible context-consistent locations (Figure 6f), indicating that both hippocampal and entorhinal context representations contribute to spatial memory. Together, these results demonstrate that in concert with hippocampal remapping, entorhinal cortex represented the Squircle using a flexible grid-like code that changed orientation consistent with contextual memory.

DISCUSSION

A major scientific challenge has been to understand how the brain processes contextual information in the service of spatial memory[29,30]. We found that while human participants performed a context-dependent object-location memory task, entorhinal grid-like representations realigned between two different navigational contexts (the Square and Circle), and coincident changes in fMRI activity patterns consistent with remapping were observed in the hippocampus. These results add to a growing body of evidence that hippocampal remapping and entorhinal grid realignment are key mechanisms by which the human brain distinguishes between navigational experiences that occur in different contexts[15–17,23]. Critically, in an ambiguous half-square half-circle context (the Squircle), fMRI proxies for hippocampal remapping and entorhinal grid realignment were predictive of

contextual memory retrieval on a trial-by-trial basis; that is, when participants retrieved Square- or Circle-consistent memories in the Squircle, context representations in the hippocampal formation were similar to those elicited in the Square or Circle, respectively. Thus, hippocampal remapping and entorhinal grid realignment mediate human contextual memory.

Hippocampal remapping and contextual memory

The hippocampus has long been hypothesized to play a central role in representing spatial context[11], a key implication of which is that context changes should modulate hippocampal representations in agreement with spatial memory. Prior studies using spatial memory tasks with rodents have found mixed results, with some observing a relationship between remapping and memory[31,32], others observing remapping but no change in memory[33], and yet others finding no remapping despite retrieval of different memories[34]. Importantly, such prior studies asked how environmental or spatial task changes affect remapping and memory independently, rather than whether remapping covaries with memory under the same conditions, making the source of potential dissociations between remapping and behavior difficult to ascertain. For instance, remapping could be observed without a change in behavior if a navigator has the opportunity to learn a new association between that behavior and the remapped context representation following environmental change.

Here we created a situation in which navigators were unable to learn new context-location associations in the Squircle, but instead had to retrieve one of two previously formed contextual memories in the same environment. We then applied a stringent test of the relationship between hippocampal activity and contextual memory: i) activity patterns must predict contextual memory on a trial-by-trial basis, and ii) context-specific activity patterns must be tolerant to changes in nonmnemonic factors that could ostensibly covary with contextual memory, such as visual input and target object identity. We found that context representations were predictive of contextual memory on a trial-by-trial basis and were tolerant to changes in nonmnemonic factors during VR-walking epochs. By applying this stringent test, the current work complements and extends previous fMRI and intracranial recording studies examining the role of the human hippocampus in contextual memory[15–17,35]. Earlier research has shown that hippocampal activity elicited during spatial memory encoding is reinstated during recall[15,35], akin to the trial-by-trial reinstatement of Square and Circle representations in the Squircle, but the sensitivity of such reinstated representations to nonmnemonic factors was not tested. Conversely, two recent studies reported tolerance of context-specific hippocampal activity patterns to changes in visual input[16,17], but did not link such activity patterns to contextual memory on a trial-by-trial basis.

Unexpectedly, we found that the hippocampus switched between view-tolerant mnemonic representations and contextual-memory-tolerant view-based representations during VR-walking and VR-stationary epochs, respectively. This observation reinforces the importance of testing the resilience of hippocampal context representations to a range of nonmnemonic factors. It is unclear if the switch between mnemonic and view-based coding was caused by changes in VR-locomotion *per se,* or changes in cognitive state that likely covary with VR-locomotory behavior, such as attending to spatial versus visual aspects of the

environment[36]. Nevertheless, our data suggest that although the hippocampus supports contextual memory, its mnemonic role is flexibly modulated by behavioral or cognitive state[37].

Hippocampal sensitivity to visual input during VR-stationary epochs dovetails with a recent human fMRI study showing hippocampal coding of allocentric VR-orientation, which covaried with view, only when participants were VR-stationary[38]. Unlike this study, however, we found that the hippocampus treated different Squircle viewing directions as similar according to whether those directions were associated with visual scenes that co-occurred in the Square or Circle, respectively. This finding is consistent with the spatiotemporal similarity hypothesis of hippocampal function[39], according to which the hippocampus represents visual scenes as similar according to their co-occurrence in space and/or time. Hippocampal tuning to contextual memory and the spatiotemporal similarity of visual inputs may both reflect the operation of the same pattern completion process[40], providing a possible mechanistic bridge between mnemonic and higher-order perceptual functions of the hippocampus.

Grid realignment and contextual memory

Entorhinal grid cells have long been hypothesized to play a role in spatial memory[41]. Yet, no previous studies have linked the global properties of a particular grid representation, such as its orientation, to memory-guided behavior. Complementing what was observed in the hippocampus, we found that realignment of entorhinal grid-like signals predicted contextual memory retrieval on a trial-by-trial basis, thus establishing a role for grid-like representations in context-dependent spatial memory.

The observation that grid-like realignment is predictive of contextual memory speaks to an ongoing debate about the function of the grid code in behavior. On the one hand, because of the repetitive nature of grid cell firing fields, the primary function of grid cells may be to encode the output of a path integration computation that confers a spatial metric to the brain's navigation system[42]. In this scenario, grid representations are context invariant, and changes to context only affect grid representations insofar as they alter the metric properties of the environment, such as changes to the shape or orientation of local space[20,43]. In this case, we would have expected grid-like representations to realign between the Squircle and both the Square and Circle, since the spatial layout differed between all three arenas. On the other hand, the grid code may serve as a high-capacity spatial representation capable of taking into account a navigator's memory for space beyond the perceived shape of the environment[44,45]. By demonstrating that the entorhinal grid code reflects contextual memory beyond the metric properties of the world when context is behaviorally relevant, our results are less consistent with the former theory. Note however that this conclusion should not be taken to imply that metric environmental properties do not anchor grid representations to the external world, as we also found that grid-like representations were oriented by the shape and orientation of local space in the Square and Circle[25–28]. A potential parsimonious explanation is that the grid system is deployed for path integration only after the global properties of a particular grid representation (e.g., its orientation) are established via a contextual memory retrieval process.

Network dynamics in entorhinal cortex are hypothesized to be a possible determinant of hippocampal remapping[46,47], and breakdown of entorhinal grid representations in a mouse model of Alzheimer's disease accompany impaired remapping and contextual memory[48]. Yet, remapping is observed in rodents even following complete lesions to the entorhinal grid system[49], challenging the role of hippocampal-entorhinal interactions, and entorhinal cortex more broadly, in contextual memory separation. We found that when grid realignment and hippocampal remapping predicted retrieval of different contextual memories in the Squircle, participants recalled target objects as being located closer to the location intermediate between the two possible context-consistent locations. This suggests that when the hippocampus and entorhinal cortex encode different context representations, rather than retrieve a single contextual memory, participants may have been more likely to adopt a navigational strategy whereby information from both the Square and Circle are combined to recall target object location[50]. Coherence between hippocampal and entorhinal context representations is thus critical for retrieval of context-specific memories: either because there is a constructive interaction between the two brain regions or because incoherence can cause interference between signals arising from the two brain regions.

Conclusions

In sum, we found that while human participants performed a context-dependent spatial memory task, fMRI proxies for hippocampal remapping and entorhinal grid-like realignment predicted contextual memory retrieval on a trial-by-trial basis. These results help to close the gap between rodent and human studies of contextual memory and validate the long-held theory that a critical function of the hippocampal formation is to represent the contextual information that guides spatial behavior.

ACKNOWLEGMENTS

We thank L. Sommer and L. Sandøy for help with data collection, and M. Nau for discussions. This study was supported by the European Research Council (ERC-CoG GEOCOG 724836). We acknowledge further support to CFD from the Max Planck Society; the Netherlands Organisation for Scientific Research (NWO-Vidi 452-12-009); the Kavli Foundation, the Centre of Excellence scheme of the Research Council of Norway – Centre for Neural Computation (223262/F50), The Egil and Pauline Braathen and Fred Kavli Centre for Cortical Microcircuits, the National Infrastructure scheme of the Research Council of Norway – NORBRAIN (197467/F50), and NTNU.

AUTHOR CONTRIBUTIONS

Conceptualization, J.B.J and C.F.D.; Methodology, J.B.J; Investigation, J.B.J; Writing – Original Draft, J.B.J.; Writing – Review & Editing, J.B.J and C.F.D.; Funding Acquisition, C.F.D; Supervision, C.F.D

Competing Interest Statement

The authors declare no competing interests.

REFERENCES

1. El Haj, M. & Kessels, R. P. Context memory in Alzheimer's disease. *Dementia and geriatric cognitive disorders extra* **3**, 342–350 (2013).
2. Chun, M. M. & Phelps, E. A. Memory deficits for implicit contextual information in amnesic subjects with hippocampal damage. *Nature neuroscience* **2**, 844–847 (1999).
3. Colgin, L. L., Moser, E. I. & Moser, M.-B. Understanding memory through hippocampal remapping. *Trends in neurosciences* **31**, 469–477 (2008).
4. Mizumori, S. J. A context for hippocampal place cells during learning. *Hippocampal place fields: Relevance to learning and memory* 16–43 (2008).
5. Eichenbaum, H. The hippocampus and declarative memory: cognitive mechanisms and neural codes. *Behavioural brain research* **127**, 199–207 (2001).
6. Myers, C. E. & Gluck, M. A. Context, conditioning, and hippocampal rerepresentation in animal learning. *Behavioral neuroscience* **108**, 835 (1994).
7. Nadel, L. The hippocampus and context revisited. *Hippocampal place fields: Relevance to learning and memory* **1**, 3–15 (2008).
8. O'Keefe, J. & Nadel, L. *The hippocampus as a cognitive map*. vol. 3 (Clarendon Press Oxford, 1978).
9. Ranganath, C. Binding items and contexts: The cognitive neuroscience of episodic memory. *Current Directions in Psychological Science* **19**, 131–137 (2010).
10. Hirsh, R. The hippocampus and contextual retrieval of information from memory: A theory. *Behavioral biology* **12**, 421–444 (1974).
11. Julian, J. B. & Doeller, C. F. Context in spatial and episodic memory. in *The Cognitive Neurosciences* 219–234 (MIT Press, 2019).
12. O'Keefe, J. & Dostrovsky, J. The hippocampus as a spatial map. Preliminary evidence from unit activity in the freely-moving rat. *Brain research* **34**, 171–175 (1971).

13. Alme, C. B. *et al.* Place cells in the hippocampus: eleven maps for eleven rooms. *Proceedings of the National Academy of Sciences* **111**, 18428–18435 (2014).
14. Leutgeb, S., Leutgeb, J. K., Treves, A., Moser, M.-B. & Moser, E. I. Distinct ensemble codes in hippocampal areas CA3 and CA1. *Science* **305**, 1295–1298 (2004).
15. Kyle, C. T., Stokes, J. D., Lieberman, J. S., Hassan, A. S. & Ekstrom, A. D. Successful retrieval of competing spatial environments in humans involves hippocampal pattern separation mechanisms. *eLife* **4**, e10499 (2015).
16. Steemers, B. *et al.* Hippocampal Attractor Dynamics Predict Memory-Based Decision Making. *Current Biology* **26**, 1750–1757 (2016).
17. Stokes, J., Kyle, C. & Ekstrom, A. D. Complementary roles of human hippocampal subfields in differentiation and integration of spatial context. *Journal of cognitive neuroscience* **27**, 546–559 (2015).
18. Witter, M. P. & Amaral, D. G. The hippocampal region. *The rat nervous system* 637–703 (2004).
19. Diehl, G. W., Hon, O. J., Leutgeb, S. & Leutgeb, J. K. Grid and nongrid cells in medial entorhinal cortex represent spatial location and environmental features with complementary coding schemes. *Neuron* **94**, 83–92 (2017).
20. Fyhn, M., Hafting, T., Treves, A., Moser, M.-B. & Moser, E. I. Hippocampal remapping and grid realignment in entorhinal cortex. *Nature* **446**, 190–194 (2007).
21. Hafting, T., Fyhn, M., Molden, S., Moser, M.-B. & Moser, E. I. Microstructure of a spatial map in the entorhinal cortex. *Nature* **436**, 801–806 (2005).
22. Doeller, C. F., Barry, C. & Burgess, N. Evidence for grid cells in a human memory network. *Nature* **463**, 657–661 (2010).
23. Nadasdy, Z. *et al.* Context-dependent spatially periodic activity in the human entorhinal cortex. *Proceedings of the National Academy of Sciences* **114**, E3516–E3525 (2017).

24. Ainge, J. A., Dudchenko, P. A. & Wood, E. R. Context-dependent firing of hippocampal place cells: Does it underlie memory. *Hippocampal place fields: Relevance to learning and memory* 44–58 (2008).
25. He, Q. & Brown, T. I. Environmental Barriers Disrupt Grid-like Representations in Humans during Navigation. *Current Biology* **29**, 2718–2722 (2019).
26. Julian, J. B., Keinath, A. T., Frazzetta, G. & Epstein, R. A. Human entorhinal cortex represents visual space using a boundary-anchored grid. *Nature neuroscience* 1 (2018).
27. Krupic, J., Bauza, M., Burton, S., Barry, C. & O'Keefe, J. Grid cell symmetry is shaped by environmental geometry. *Nature* **518**, 232–235 (2015).
28. Stensola, T., Stensola, H., Moser, M.-B. & Moser, E. I. Shearing-induced asymmetry in entorhinal grid cells. *Nature* **518**, 207–212 (2015).
29. Davies, G. M. & Thomson, D. M. *Memory in context: Context in memory.* (John Wiley & Sons, 1988).
30. Nadel, L. & Willner, J. Context and conditioning: A place for space. *Physiological Psychology* **8**, 218–228 (1980).
31. Schimanski, L. A., Lipa, P. & Barnes, C. A. Tracking the Course of Hippocampal Representations during Learning: When Is the Map Required? *J. Neurosci.* **33**, 3094–3106 (2013).
32. Kennedy, P. J. & Shapiro, M. L. Motivational states activate distinct hippocampal representations to guide goal-directed behaviors. *Proceedings of the National Academy of Sciences* **106**, 10805–10810 (2009).
33. Jeffery, K. J., Gilbert, A., Burton, S. & Strudwick, A. Preserved performance in a hippocampal-dependent spatial task despite complete place cell remapping. *Hippocampus* **13**, 175–189 (2003).

34. Bower, M. R., Euston, D. R. & McNaughton, B. L. Sequential-context-dependent hippocampal activity is not necessary to learn sequences with repeated elements. *Journal of Neuroscience* **25**, 1313–1323 (2005).
35. Miller, J. F. *et al.* Neural activity in human hippocampal formation reveals the spatial context of retrieved memories. *Science* **342**, 1111–1114 (2013).
36. Nau, M., Julian, J. B. & Doeller, C. F. How the brain's navigation system shapes our visual experience. *Trends in cognitive sciences* (2018).
37. Gulli, R. A. *et al.* Context-dependent representations of objects and space in the primate hippocampus during virtual navigation. *Nature neuroscience* **23**, 103–112 (2020).
38. Nau, M., Schröder, T. N., Frey, M. & Doeller, C. F. Behavior-dependent directional tuning in the human visual-navigation network. *Nature communications* **11**, 1–13 (2020).
39. Turk-Browne, N. B. The hippocampus as a visual area organized by space and time: A spatiotemporal similarity hypothesis. *Vision research* **165**, 123–130 (2019).
40. Yassa, M. A. & Stark, C. E. Pattern separation in the hippocampus. *Trends in neurosciences* **34**, 515–525 (2011).
41. Moser, M.-B., Rowland, D. C. & Moser, E. I. Place cells, grid cells, and memory. *Cold Spring Harbor perspectives in biology* **7**, a021808 (2015).
42. McNaughton, B. L., Battaglia, F. P., Jensen, O., Moser, E. I. & Moser, M.-B. Path integration and the neural basis of the 'cognitive map'. *Nature Reviews Neuroscience* **7**, 663–678 (2006).
43. Marozzi, E., Ginzberg, L. L., Alenda, A. & Jeffery, K. J. Purely translational realignment in grid cell firing patterns following nonmetric context change. *Cerebral Cortex* **25**, 4619–4627 (2015).
44. Mathis, A., Herz, A. V. & Stemmler, M. Optimal population codes for space: grid cells outperform place cells. *Neural computation* **24**, 2280–2317 (2012).

45. Sreenivasan, S. & Fiete, I. Grid cells generate an analog error-correcting code for singularly precise neural computation. *Nature neuroscience* **14**, 1330 (2011).
46. Latuske, P., Kornienko, O., Kohler, L. & Allen, K. Hippocampal remapping and its entorhinal origin. *Frontiers in Behavioral Neuroscience* **11**, 253 (2018).
47. Monaco, J. D. & Abbott, L. F. Modular realignment of entorhinal grid cell activity as a basis for hippocampal remapping. *Journal of Neuroscience* **31**, 9414–9425 (2011).
48. Jun, H. *et al.* Disrupted Place Cell Remapping and Impaired Grid Cells in a Knockin Model of Alzheimer's Disease. *Neuron* (2020).
49. Schlesiger, M. I., Boublil, B. L., Hales, J. B., Leutgeb, J. K. & Leutgeb, S. Hippocampal Global Remapping Can Occur without Input from the Medial Entorhinal Cortex. *Cell reports* **22**, 3152–3159 (2018).
50. Xu, Y., Regier, T. & Newcombe, N. S. An adaptive cue combination model of human spatial reorientation. *Cognition* **163**, 56–66 (2017).

METHODS

Participants

24 participants (14 female) took part in this experiment (mean age: 26; range: 20-34). All participants gave written consent and were paid for participating with a standardized financial incentive (120 NOK/hour), in compliance with procedures approved by the regional committees for medical and health research ethics (REK sør-øst; protocol reference: 2017/1900). All had normal vision and reported to be in good health with no history of neurological disease. Data from two additional participants were collected but discarded before analysis of fMRI data, one due to chance-level performance during testing and one due to technical errors during fMRI data acquisition. A further two participants were excluded from the study prior to fMRI scanning due to an inability to learn the behavioral task during training. The study was a within-subject design and thus there was no randomization of groups or treatments; further, because the study was a within-participant design with no treatment, data collection and analysis were not performed blind to the conditions of the experiments.

Behavioral task

Virtual Environment. We used Python to construct a virtual-reality environment that was rendered and displayed from the first person-perspective using the Vizard VR toolkit 3.0. The virtual environment consisted of three separate arenas, one square ("Square"), one circular ("Circle"), and one half-square half-circle ("Squircle"). In each arena, the boundary wall was 2.34 virtual meters (vm) in height relative to a simulated eye-level of 1.82 vm. The diameter of the Circle was 29 vm and the length of one wall in the Square was 29 vm. The Square and Circle were each surrounded by four distal cues, offset from each other within a context by 90°. The identities of the distal cues were counterbalanced across contexts across participants. The Squircle arena was surrounded by all eight distal cues, four from the Square and four from the Circle. Relative to the Squircle reference frame, Square and Circle distal cues were rotated relative to each other 54°, which allowed us to differentially test whether entorhinal grid-like orientations were aligned to the distal cues in the Square and Circle, and to the boundaries in the Square (see ***Grid-like analyses*** below). During the task, a participant's location and facing direction (relative to an arbitrary east direction, which was the same for the Circle and Square relative to the distal cues in the Squircle reference frame) was recorded at 20 Hz.

Training procedure. During behavioral training prior to the fMRI experiment and outside of the MR environment, participants navigated through the arena using their left hand to operate keys to move forward and turn left or right. At the start of behavioral training, participants were instructed that they would learn object locations in two different arenas, one square and one circle. They were then briefly exposed to both the Square and Circle during a free exploration period in each context. Following free exploration, training involved learning the locations of four everyday target objects (pumpkin, potted plant, lamp, and traffic cone) within the Circle and Square. The object identities were the same in the Circle and Square but occupied different locations (x- and y-coordinates relative to [0,0] center: Circle=[-4,9; 2,5; -7,-4; 10,-5]; Square=[4,9; -2,5; 7,-4; -10,-5]). The positions of the target objects were

the same for each participant and were mirror symmetric across the two contexts. No participant reported noticing this mirror symmetry during debriefing following the experiment. Each trial began with the display of a word denoting one of the test objects. Participants then navigated to the remembered location of that object from a random starting point (the “recall” phase). When they reached their goal, they made a button press response. Participants were given feedback, and after a 2s delay, the target object for that trial appeared at its correct location and was collected (the “feedback” phase). Feedback ranged continuously from strongly negative (red frown face) if a participant recalled the object’s location greater than 8vm from the correct location, to strongly positive (green smile face) if the recalled object location was less than 3vm from the correct location. A set of 16 trials (four per experimental object) composed a block, and memory for object locations was trained in each arena in a separate block of trials. The order in which the arenas were trained across blocks was counterbalanced across participants.

Prior to the start of the first recall phase during training block 1 for each context, but not subsequent blocks, participants collected each object in pseudorandom order twice (i.e., performed the feedback phase twice per test object) to initially learn the locations of the objects. Within a block, memory for the object locations was assessed in pseudorandom order, with the constraint that memory for the same object location could not be tested until all other objects had been tested once. Each participant was trained for four training blocks per context, with three training blocks per context occurring approximately five days before fMRI scanning, and one top-up training block per context occurring immediately before fMRI scanning.

Testing procedure. Following behavioral training outside of the MRI scanner, participants performed the recall phase in the three testing arenas (Square, Circle, Squircle) while undergoing fMRI scanning. There was a pseudorandom 2-5s intertrial interval, during which a word denoting the test object for the subsequent trial was displayed. At the start of each trial, participants were teleported to a pseudo-random position in the arena, with the constraint that teleport locations in each arena were restricted to the boundaries of the Circle (i.e., in the Square and Squircle, participants never began a trial near the square corners). This teleportation restriction was included to maximize the likelihood that sampling of arena locations was similar in each context. Immediately following teleportation at the start of each trial, participants were automatically rotated fully around once (360º; 12s duration), so that they had an initial opportunity to identify their context and to minimize the possibility that they would fail to identify that they were in the Squircle on Squircle trials. Following this rotation period, participants navigated through the arena using a button-box to move forward and turn left or right. The order in which arenas were tested during scanning across trials was pseudo-random with the constraint that both the Square and Circle were tested twice each, and the Squircle tested once, every five trials. Memory for the target object locations in each testing arena was examined in pseudo-random order, with the constraint that each target object was tested once every four trials. Testing was divided into eight 8.075 minute (475 acquisitions) scan runs. Due to technical issues with the stimulus display computer, two participants completed only 7 total scan runs. Since testing was self-paced, the number of trials completed per context differed across participants (means=[51, 50, 24], medians=[51, 51, 24]; ranges=[31-72, 29-71, 13-32]; standard

deviations=[7.77,7.40,3.13] completed trials in the Square, Circle, and Squircle, respectively). However, since each scan run had a fixed length, the number of fMRI acquisitions for each context per scan run was highly similar across participants (standard deviations in the number of fMRI acquisitions per run expressed as a percentage of the total scan run length: [2.4,3.3,2.9] in the Square, Circle, and Squircle, respectively).

Unlike training, no feedback was provided following each test trial. However, to maintain participant attention during scanning, feedback was provided at the end of each scan run based on the average performance in the Square and Circle during that run. If 475 fMRI volumes were acquired prior to completion of the last trial of a given scan run, participants completed that last trial and received performance feedback prior to the start of the subsequent scan run.

(f)MRI data acquisition

Scanning was performed at St. Olavs Hospital at the Neuro Center (Nevrosenteret) using a 3-Tesla Siemens Skyra scanner equipped with a 32-channel head coil. High-resolution T1-weighted images for anatomical localization were acquired at the start of each scan session using a 3-dimensional magnetization-prepared rapid-acquisition gradient-echo pulse sequence (repetition time [TR], 1900 ms; echo time [TE], 3.16 ms; inversion time, 900 ms; flip angle 9°; voxel size, 1x1x1 mm; matrix size, 256x256x192). T2*-weighted images sensitive to blood oxygenation level-dependent (BOLD) contrasts were acquired using a gradient-echo echoplanar pulse sequence (TR, 1020 ms; TE, 34.6 ms; flip angle 55°; voxel size, 2.02x2.02x2 mm; matrix size, 104x104x66; multiband acceleration factor of 6). Functional image slices were aligned approximately parallel to the long axis of hippocampus. To correct susceptibility induced distortions, after completion of all experimental scan runs for 22/24 participants, a single T2*-weighted image sensitive to BOLD contrasts was also acquired using an identical gradient-echo echoplanar pulse sequence as the main experimental runs (TR, 1020 ms; TE, 34.6 ms; flip angle 55°; voxel size, 2.02x2.02x2 mm; matrix size, 104x104x66; multiband acceleration factor of 6), but with an inversed phase encoding direction. The VR environment was displayed at a rear bore face screen. Participants viewed the stimulus through a mirror attached to the head coil. Behavioral responses were collected using a fiber-optic button box.

Behavioral data analysis

Behavioral performance was measured in terms of the Euclidean distance between each target object's recalled location and the actual target object location ("distance error"). To determine the distance error expected by chance in the Square and Circle, we computed the mean distance between 1,000 evenly spaced locations in the Square (Circle) and the four actual target locations in the Square (Circle). The chance distance errors thus computed served as a baseline relative to which we compared observed distance error. To classify Squircle trials as either Square- or Circle-consistent we computed the distance between each Squircle trial's recalled location and the corresponding location of that trial's target object in the Square and Circle, respectively, and classified each Squircle trial as either Square- or Circle-consistent based on whichever context had the smaller distance error. To compute distance error expected by chance in the Squircle, for each target object, we

computed the distance between 1,000 evenly spaced locations in Squircle and the minimum distance of those locations to the Square- or Circle-consistent location, whichever context-consistent location had a smaller distance error.

To compute maps of the difference in recalled location density between Square- and Circle-consistent Squircle trials (Figure 2c), for each participant and target object, we constructed a map of Squircle recalled locations (map resolution: 0.5vm; % total trials per object), separately for Sq- and Ci-consistent trials. For each target object, we then took the difference between Sq- and Ci-consistent maps, smoothed the difference maps with a Gaussian kernel (σ=2vm), and averaged each object's map across participants.

We also tested whether VR-walking trajectories reliably differed in shape between contexts (procedure depicted schematically in Extended Data Figure 2i). For each participant, for each possible pair of VR-walking trajectories T1 and T2, we first interpolated T2 using a spline fit so that it contained the same number of points as T1. To account for differences in each trajectory's starting and ending location, T2 was translated so as to have the same starting location as T1 and then a Procrustes transformation was performed to maximally align T2 to T1. Finally, we computed the discrete Fréchet distance[51] between T1 and T2, which corresponds to a measure of similarity between the two trajectories that takes into account both the location and ordering of the points along the trajectories.

fMRI data analysis

FMRI data analyses were performed on the Abel Cluster, owned by the University of Oslo and Uninett/Sigma2, and operated by the Department for Research Computing at USIT, the University of Oslo IT-department (www.hpc.uio.no).

***Preprocessing*.** All imaging data were preprocessed using software tools developed and distributed by FreeSurfer (v6.0.0; surfer.nmr.mgh.harvard.edu) and FMRIB's Software Library (FSL; v5.0.11; fsl.fmrib.ox.ac.uk/fsl). Cortical surface gray-white matter volumetric segmentation of the high-resolution anatomical image was performed using the 'recon-all' utility in the FreeSurfer analysis suite. Segmented T1 data were used to define ROIs for use in subsequent analyses, as described below. Functional data were motion corrected using the FSL tool MCFLIRT, a final sinc interpolation stage, and 6 degrees of freedom. Slow drifts in the functional data were removed using highpass temporal filtering (Gaussian-weighted least-squares straight line fitting, with sigma=50.0s). Susceptibility distortions were removed using the FSL tool Topup. Non-brain was then removed from the first volume of every functional run using FSL's BET, and brain-extracted volumes were registered to the segmented anatomical image. Transformation matrices for registration were generated using FreeSurfer's manual and boundary-based registration tools. These matrices were then used to transform each four-dimensional functional volume using FSL FLIRT, such that all cross-run data from a single participant were in the same space. For univariate analyses, functional data were spatially smoothed using a Gaussian kernel of 5mm FWHM. Spatial smoothing procedures for multivariate analyses are described below. For second-level group analyses, functional data were normalized into standard space (MNI305) with FreeSurfer using non-linear registration.

Regions of interest*.* Anatomical regions of interest (ROI) were defined uniquely for each participant based on the automatic cortical and subcortical parcellations derived from FreeSurfer structural reconstruction. These ROIs included the bilateral hippocampus (HIPP), bilateral entorhinal cortex (EC), and bilateral pericalcarine cortex (which we refer to here as early visual cortex—EVC), all drawn from the Desikan-Killiany atlas[52]. Example hippocampal and entorhinal ROIs are depicted in Supplementary Figure 1a. To determine the anatomical locus of multivariate context representations, we also divided each participant's hippocampal ROI into three subregions of interest[53] along its posterior-anterior extent (posterior, middle, anterior), separately for each hemisphere, such that each subregion had the same length in the posterior-anterior dimension. For multivariate context decoding only, we also divided each participant's EC ROI into two parts along its poster-anterior extent (posterior, anterior), separately for each hemisphere (Supplementary Figure 1b).

Multivariate context decoding. Multivariate analyses were performed using FSL (v5.0.11) and Matlab (v2017b). We reasoned that if remapping causes different hippocampal populations to be active in the Square and Circle there would be reliably different fMRI activity patterns elicited during navigation episodes in each context. Note that this claim does not require information about a navigator's spatial location within a context to be decodable from the multivariate hippocampal fMRI signal, which may not be feasible given the spatial resolution limitations of fMRI[54]. For each scan run, we used a general linear model (GLM) to estimate the response of each voxel to the recall phase separately for each context. Run-wise GLMs consisted of two binary boxcar regressors: one for the recall phase in the Square and one for the Circle. Also included in each GLM were six nuisance parametric modulators (PMs) to account for head motion-related artifacts and their temporal derivatives. All regressors were convolved with double gamma hemodynamic response function (HRF) and filtered by the same high pass filter as the fMRI data before entry into the GLM. GLMs were performed in FSL using FILM with local autocorrelation correction. Run-wise parameter estimates thus obtained were spatially smoothed using a Gaussian kernel of 4 mm FWHM.

For Square versus Circle context decoding (Figure 3a), we then created run-wise activity patterns for the Square and Circle contexts by concatenating response values across all hippocampal voxels. For each run, patterns were *Z*-scored across voxels. Context classification accuracy was determined using leave-one-run-out cross validation. Specifically, we first performed voxel selection to identify hippocampal voxels modulated by context, such that only voxels exhibiting a response difference between the Square and Circle contexts (liberal threshold $p<0.1$, uncorrected) were included in these concatenated patterns. To avoid statistical dependence between this voxel selection procedure and subsequent classifier-based analyses, voxel selection was performed in a leave-one-run-out fashion. That is, for each participant, a held-out run's hippocampal mask was constructed solely on the basis of context-related activations from the remaining scan runs (Supplementary Figure 2). For each run-wise partition of the data, we then averaged the patterns across the non-held-out data across runs, separately for the Square and Circle, and compared these patterns to each volume of fMRI data in the held-out run. Functional data in the held-out run were smoothed using a Gaussian kernel of 4mm FWHM, and signal amplitude timeseries were normalized via *Z*-scoring across time for

each voxel, and then across voxels in an ROI for each volume. Each fMRI volume in each held-out run was then classified as Square or Circle based on whichever context yielded higher pattern similarity (Fischer-transformed Pearson correlation coefficient) to the average Square and Circle training data activity patterns, and each individual trial was classified as either Square or Circle based on the modal prediction across all fMRI volumes during each trial's recall phase. To account for the hemodynamic lag, the actual recall phase onset of each trial was shifted by 6 fMRI volumes (6.12 s), but the end of the recall phase was not offset. For Squircle contextual memory decoding (Figure 3c), we performed the same leave-one-run-out analysis, except compared the Squircle activity patterns in the held-out run to the Square and Circle context patterns in the training data. To assess classification accuracy expected by chance, we re-ran the same analysis permuting context labels across trials (k=500).

To examine the evolution of the context representations for each volume of fMRI data in each held-out scan run (Figure 3b and d), we computed a Contextual Similarity (CS) Score corresponding to the difference in pattern similarity strength (Fischer-transformed Pearson correlation coefficient) between each volume's activity pattern and the average patterns elicited in the Square minus the Circle across runs. Since different trials could be of different length, CS Scores for each trial were resampled to 30 timepoints using the *resample* function in Matlab. To account for the hemodynamic lag, the actual recall phase onset of each trial was shifted by 6 fMRI volumes (6.12 s), but the end of the recall phase was not offset. CS Scores were separately computed for the pre-recall phase rotation period and consisted of the 12 fMRI volumes prior to the recall phase. The start and end of the rotation period were both offset by 6 fMRI volumes, such that the end of the rotation period corresponded to the fMRI volume immediately prior to the start of the recall phase. As a control, we also repeated the same analyses for the EVC ROI. To determine the anatomical locus of these effects, we also performed the same analyses in the hippocampal and entorhinal subregion ROIs without voxel selection (Figure 3e and f).

We then tested the sensitivity and tolerance of Squircle hippocampal context representations to nonmnemonic factors:

VR-locomotory behavior (Figure 4a-b). Each CS Score timeseries was binned into VR-walking and VR-stationary epochs. Each fMRI volume during which the mean VR-walking velocity 6 fMRI volumes (6.12 s) earlier was greater than 1.65 vm/s were included in VR-walking epochs, and all other fMRI volumes were included in VR-stationary epochs. This VR-walking velocity cutoff was used to ensure that participants were VR-walking for the majority of each fMRI volume included in VR-walking epochs (3.3 vm/s is full speed).

VR-walking location (Figure 4c-d). The Squircle environment was divided into a map of 49 equally spaced locations. This map resolution (8.3 vm^2 area bins) was selected because each location bin corresponds to the approximate maximum distance that could be VR-traversed during a single fMRI acquisition. Mean CS Scores were then computed separately for each location based on the participant's VR-walking location 6 fMRI volumes (6.12 s) earlier. Individual participant CS Score maps were Gaussian smoothed (σ=8vm) before averaging across participants. We also tested whether context representations were tolerant to proximity to square vs. circular

boundary segments in the same manner as we did for VR-locomotion by binning CS Score timeseries based on the most proximal boundary segment type (square or circular corner) 6 fMRI volumes (6.12 s) earlier.

viewing direction (Figure 4e-j). For each fMRI acquisition, we computed the circular mean viewing direction during that acquisition, and CS Scores were then binned according to whether the participant's viewing angle 6 fMRI volumes (6.12 s) earlier was more centered on a square or circular boundary segment (Figure 4e and 4g), or a Square or Circle distal cue (Figure 4f and 4h).

Target object identity (Figure 4 & Extended Data Figure 7). We recomputed Squircle CS Scores using an alternate target-object-invariant context classifier. For each scan run, we used four separate GLMs to estimate the responses of each voxel to the Square and Circle recall phases. These GLMs were conducted in an identical fashion as the original context classifier, except that each run-wise GLM consisted of two binary boxcar regressors (one for the Square and one for the Circle) that each excluded all trials from one of the four target objects. Thus, four sets of run-wise parameter estimates were obtained for the Square and Circle, each derived using all trials except for those from one specific target object each (i.e., exclude-pumpkin, exclude-plant, exclude-lamp, and exclude-cone). Parameter estimates thus obtained were spatially smoothed using a Gaussian kernel of 4 mm FWHM. We then recomputed CS Score timeseries for each Squircle trial by applying the particular classifier that excluded that Squircle trial's target object. For instance, if the target object for a given Squircle trial was the pumpkin, target-object-invariant CS Scores were computed for that trial using the exclude-pumpkin parameter estimates.

Grid-like analyses. Grid-like analyses were performed using FSL (v5.0.11) and Matlab (v2017b). We first performed a split-half quadrature filter analysis to estimate the context-specific orientations of the grid code during periods of VR-walking in the Square and Circle (Figure 5), following now-standard procedures[22]. In brief, for each scan run, we identified the context-specific angular orientation of the putative grid axes in each participant's entorhinal cortex (EC). Data were then split into halves by run (runs [1,3,5,7] and [2,4,6,8] for n=22 participants, and runs [1,3,5,7] and [2,4,6] for n=2 participants missing the 8th scan run), and for each half, we computed the circular average grid-like orientation separately for the Square and Circle contexts. The grid-like orientations thus obtained were then subsequently used to predict a grid-like signal during the other independent half of the runs. For all grid-like analyses described below, in addition to the PMs of interest, GLMs also included six nuisance PMs to account for head motion-related artifacts, as well as two binary boxcar regressors of no interest corresponding to the Circle- and Square-consistent Squircle recall phases. All regressors were convolved with a double gamma HRF and filtered by the same high pass filter as the fMRI data before entry into the GLM. GLMs were performed in FSL using FILM with local autocorrelation correction.

To fit the orientation of the 6-fold VR-walking direction-modulated signal within EC, we constructed a GLM with four parametric modulators (PMs) for periods. These four PMs were $\cos(6*\Theta(t)_{square})$, $\cos(6*\Theta(t)_{circle})$ and $\sin(6*\Theta(t)_{square})$, $\sin(6*\Theta(t)_{circle})$, where $\Theta(t)_C$ is the VR-walking direction sampled at time t in context C. The weights (b_1–b_4, respectively) on these four PMs were fitted to the fMRI time series for each voxel within the bilateral entorhinal ROI. Since our primary goal was to test the

relationship between grid-like realignment and contextual memory in the Squircle, we sought to limit the influence of voxels with relatively weak fMRI signal from this grid orientation computation. For each participant, we thus identified the 80% of EC voxels that showed the highest magnitude of 6-fold periodic modulation in the Square and Circle averaged across scan runs, independent of grid orientation reliability across scan runs or realignment between contexts. This 80% cutoff was chosen because the bottom 20% of EC voxels had a comparatively low tSNR in all participants (Supplementary Figure 3). Note that our test of grid-like modulation (split-half reliability) was not biased by this voxel-selection procedure, nor was our test of Square and Circle grid realignment, nor were any Squircle analyses. We then used these sub-selected voxels to calculate the mean context-specific orientations of the 6-fold symmetric VR-walking direction-modulation from the mean weights as $\varphi_{square}=[\arctan(b_3/b_1)]/6$ and $\varphi_{circle}=[\arctan(b_2/b_4)]/6$, separately for each scan run, where arctan was mapped into 360° space. Finally, we computed the circular average grid orientation for each context for each separate half of the data.

Rather than use voxel selection to limit the influence of weakly modulated EC voxels, some prior studies have used an EC ROI consisting only of the posterior portion of EC (pEC)[55]. Since the anatomical specificity of the link between contextual memory and grid realignment, insofar as it exists, is not known *a priori*, we focused analyses on the entire bilateral EC, only excluding voxels with weak grid-like signal overall independent of anatomical location. Nevertheless, to confirm that our results would be similar if we instead used the pEC without voxel selection, we recomputed grid orientations using all voxels in bilateral pEC. Across participants, grid orientations in the pEC, circularly averaged across voxels and scan runs, were highly similar to grid orientations computed with voxel selection (circular correlation, n=24, φ_{square}: c=0.607, p=0.006; φ_{circle}: c=0.606, p=0.006). Further, across participants, a greater percentage of pEC voxels shared a similar grid orientation (within ±15°) across data halves within the same context than across data halves across different contexts (n=24, sign-test, p=0.032), confirming that grid realignment did not depend on our voxel selection procedure.

To test whether the fit orientations predicted analogous 6-fold periodic signals in the other independent half of the data (Figure 5b-c), we constructed a GLM with two PMs modeling the effect of VR-walking direction on the fMRI signal, one for the Square and one for the Circle. The values of these PMs at each timepoint was the cosine of VR-walking direction at that timepoint aligned to the context-specific orientation predicted by the first half of the data: $\cos(6*(\Theta(t)_{square}- \varphi_{square}))$ and $\cos(6*(\Theta(t)_{circle}-\varphi_{circle}))$. Each beta from this analysis reflects the extent of split-half reliable context-specific φ-oriented 6-fold VR-walking direction-modulated fMRI signal (which we term “grid-like modulation”). The beta weights for these PMs were averaged across all scan runs within each participant. The group-level test of the significance of these weights averaged across contexts was small-volume FWE-corrected (SVC) within a group-level bilateral EC ROI, defined as the union of all individual-participant bilateral EC ROIs projected into MNI space. To test for grid-like realignment between the Square and Circle contexts, we separately performed an analogous GLM in which VR-walking directions at each timepoint were aligned to the orientation from the opposite context, as $\cos(6*(\Theta(t)_{square}- \varphi_{circle}))$ and $\cos(6*(\Theta(t)_{circle}-\varphi_{square}))$. To confirm that the VR-walking direction-modulated signal in EC exhibited a specifically 60° periodicity, we conducted this same split-half analysis for 90° (i.e., 4-

fold) and 45° (i.e., 8-fold) periodicities (Extended Data Figure 8a). We also performed the same split-half analysis on the hippocampus and EVC ROIs (Extended Data Figure 8b-c).

To test whether grid orientations consistently cluster across participants around an offset of ±7.5° from the cardinal axes of the boundaries of the Square arena (Extended Data Figure 9), we computed the circular average of the Square grid orientations across all EC voxels and runs within each participant. We then folded the grid orientations of all participants by φ mod 15°, which would align all hypothesis-consistent alignments to 7.5° in a circular 0°-15° space in the Square. Next, we performed a V-test for nonuniformity centered around 7.5°. To test whether grid orientations were consistently aligned relative to the distal cues across participants in either the Square or Circle—either directly aligned 0° or maximally offset 45° relative to a distal cue—we performed an analogous analysis, but performed the V-test centered around 12° for Square grid orientations, and 3° for Circle grid orientations, after folding grid orientations of all participants by φ mod 15°.

To test whether grid-like representations realign on a trial-by-trial basis consistent with contextual memory in the Squircle (Figure 6b and d), we compared two grid-like models of EC activity during Squircle trials (memory-consistent vs. memory-inconsistent). Both models consisted of a single PM: $\cos(6*(\Theta(t)_{squircle} - \varphi_{(in)consistent}))$, where $\Theta(t)_{squircle}$ corresponds to the VR-walking direction at each time point t, and $\varphi_{(in)consistent}$ corresponds to the Square or Circle grid orientation, whichever was consistent or inconsistent with contextual memory retrieval for each Squircle trial, respectively. For this analysis, grid orientations were computed as the circular average of grid orientations across all scan runs within each participant, separately for the Square and Circle. Each model was fit to the fMRI data in a separate GLM. The beta weights thus obtained were averaged across all scan runs for each voxel for each participant, and then across all voxels in bilateral EC within each participant.

Since predictions of the memory-consistent and -inconsistent grid-like models were positively correlated in some participants (mean: r=0.07, range: r=-0.89-0.99), we performed a variance partitioning analysis to determine the unique contribution of each model to EC activity (Figure 6c). For each participant and scan run, we first conducted a GLM to remove nuisance variance associated with head motion-related artifacts from the EC timeseries. For each participant, we then extracted the mean EC timeseries over the course of the experiment by averaging the residuals from this GLM across all voxels in bilateral EC for each fMRI volume in each scan run. Finally, we computed the partial correlation between the memory-(in)consistent PM and the mean EC timeseries during Squircle trials, controlling for variance associated with the other PM. Both PMs were convolved with double gamma HRFs before computing the partial correlation. We also computed the amount of EC variance explained by each model uniquely (squared partial correlation coefficient – R^2), as well as the amount of EC variance explained jointly by both models together. Note that if grid orientations realign 30° across the Square and Circle, both the memory-consistent and -inconsistent models would explain equal amounts of EC variance (R^2) for the same Squircle trial, but the unsquared correlation coefficients would be of opposite sign. However, only positive correlations between a given model's PM and the EC timeseries are meaningful, as negative correlations imply systematic

misalignment of the grid orientation relative to the VR-walking direction. Therefore, for each participant, we computed the percentage of total variance explained by positive correlations only by setting each negative correlation coefficient to zero.

To examine whether trial-by-trial grid-like realignment in the Squircle was sufficient to decode contextual memory (Figure 6e), we constructed two alternative PMs to describe EC activity during each Squircle trial, one with the Square grid orientation [$\cos(6*(\Theta(t)_{squircle} - \varphi_{square})$] and one with the Circle grid orientation [$\cos(6*(\Theta(t)_{squircle} - \varphi_{circle})$]. Each PM was convolved with a double gamma HRF. For each Squircle trial's recall phase, the similarity between each PM and the de-noised average EC timeseries was computed using Spearman Rank correlation. We then classified each Squircle trial as either Square- or Circle-consistent based on whichever PM yielded a higher correlation coefficient. To assess contextual memory classification accuracy expected by chance, we re-ran this same decoding analysis permuting the contextual memory labels across Squircle trials (k=500).

To characterize whether trial-by-trial Squircle spatial memory precision was affected by whether the EC and hippocampus shared similar contextual representations (Figure 6f), we concatenated all Squircle trials across all participants. For each Squircle trial, we determined whether the contextual memory decoded in EC and the hippocampus was the same or different (i.e., either both Square or Circle, or different; $P_{EC\text{-}HIPP}$), independent of contextual memory. Trial-by-trial spatial memory precision was measured in terms of i) distance of the recalled target object location to the nearest context-consistent location (D_{con}), and ii) distance of the recalled target object location to the location intermediate between the two possible context-consistent locations (D_{int}). To account for general behavioral differences across participants and target objects, D_{con} and D_{int} were separately mean-centered within participant, and then mean-centered within target object independent of participant. We performed binomial logistic regression to test the relationship between $P_{EC\text{-}HIPP}$, D_{con}, and D_{int}. Since D_{con} and D_{int} were strongly correlated across trials ($r=0.70$, $p\approx0$), logistic regressions modeling $P_{EC\text{-}HIPP}$ as a function of D_{con} and D_{int} were performed separately as:

$$P_{EC-HIPP} = \{1 + \exp(-\beta_0 - \beta_1 \boldsymbol{D})\}^{-1}$$

where $\boldsymbol{D}$ corresponds to either D_{con} or D_{int}. D_{con} did not significantly characterize $P_{EC\text{-}HIPP}$ ($\chi^2=1.71$, $p=0.190$). The heatmap in Figure 6f was formed by separately binning D_{con} and D_{int} into quartiles and computing the average $P_{EC\text{-}HIPP}$ for each bin.

General statistics. No statistical methods were used to pre-determine sample size since our spatial learning paradigm was developed to fit participant-specific memory biases that could not be known in advance, but our sample size was similar to those reported in previous publications using similar procedures[16,26]. Parametric t-tests, Pearson correlations, repeated-measures analysis of variance (rmANOVA), logistic regression, and non-parametric sign-tests, KS-tests, V-tests and permutation tests were used throughout the paper. For parametric tests, if data values failed to meet normality assumptions (Lilliefors test, $p>0.05$), non-parametric tests are reported. All t-tests were one-tailed in the direction of the stated hypothesis, unless otherwise indicated. Note that for paired and one-sample t-tests, we do not report estimates of effect size (Cohen's *d*) because it would be redundant with the reported t-statistic

($d = t/\sqrt{n}$). 95% confidence intervals (CI) are reported for significant effects (p<0.05). A Life Sciences Reporting Summary is available.

Code availability

Task code is publicly available: github.com/jbjulian/squircle_task. FMRI analyses were performed using publicly available software packages FSL and FreeSurfer. Matlab code for other analyses are available from the corresponding authors upon request.

Data availability

The unthresholded group-level statistical brain map depicted in Figure 5b is available on NeuroVault (collection: VABINDPD). Source data for the remaining figures are available at Mendeley Data (doi:10.17632/jvm3fhpjwn.1). Raw data contained in this manuscript (Figures 2-6 and Extended Data) are available from the corresponding authors upon request.

METHODS-ONLY REFERENCES

51. Alt, H. & Godau, M. Computing the Fréchet distance between two polygonal curves. *International Journal of Computational Geometry & Applications* **5**, 75–91 (1995).
52. Desikan, R. S. *et al.* An automated labeling system for subdividing the human cerebral cortex on MRI scans into gyral based regions of interest. *Neuroimage* **31**, 968–980 (2006).
53. Nielson, D. M., Smith, T. A., Sreekumar, V., Dennis, S. & Sederberg, P. B. Human hippocampus represents space and time during retrieval of real-world memories. *Proceedings of the National Academy of Sciences* **112**, 11078–11083 (2015).
54. Nolan, C. R., Vromen, J. M., Cheung, A. & Baumann, O. Evidence against the detectability of a hippocampal place code using functional magnetic resonance imaging. *eNeuro* **5**, (2018).
55. Bellmund, J. L., Deuker, L., Schröder, T. N. & Doeller, C. F. Grid-cell representations in mental simulation. *eLife* **5**, e17089 (2016).

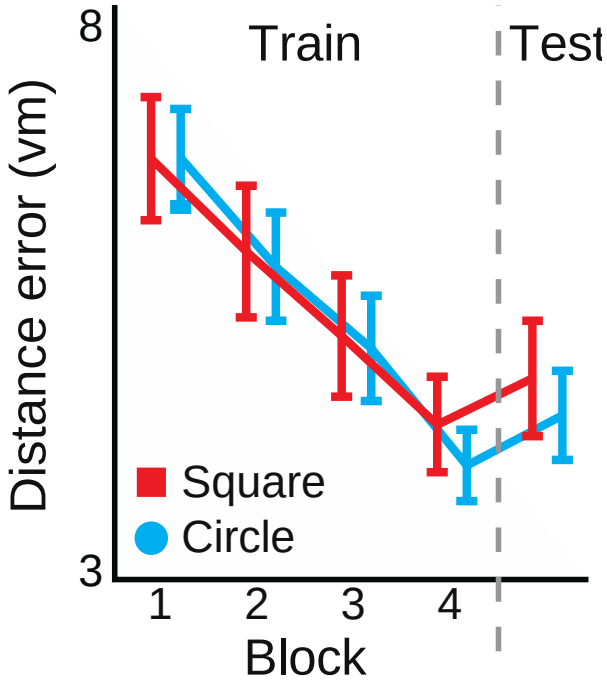

Extended Data Figure 1. Behavioral performance in the Square and Circle contexts. Performance was measured as the mean distance error in object replacement in virtual meters (vm), separately for the Square (Sq) and Circle (Ci). Performance improved across training and did not differ between the Sq and Ci at the end of training (Student's paired t-test, t_{23}=1.18, p=0.250) or during testing (t_{23}=0.95, p=0.352). Note that because the Sq had a larger walkable ground plane than the Ci, performance error expected by random chance was lower in the Ci (11.25 vm) than the Sq (13.78 vm). However, there was still no significant difference between Sq and Ci performance by training block 4 (t_{23}=1.72, p=0.098) or during testing (t_{23}=1.92, p=0.068) after normalizing distance error by the context-specific chance baseline. Error bars indicate ±1 SEM (n=24). All t-tests two-tailed.

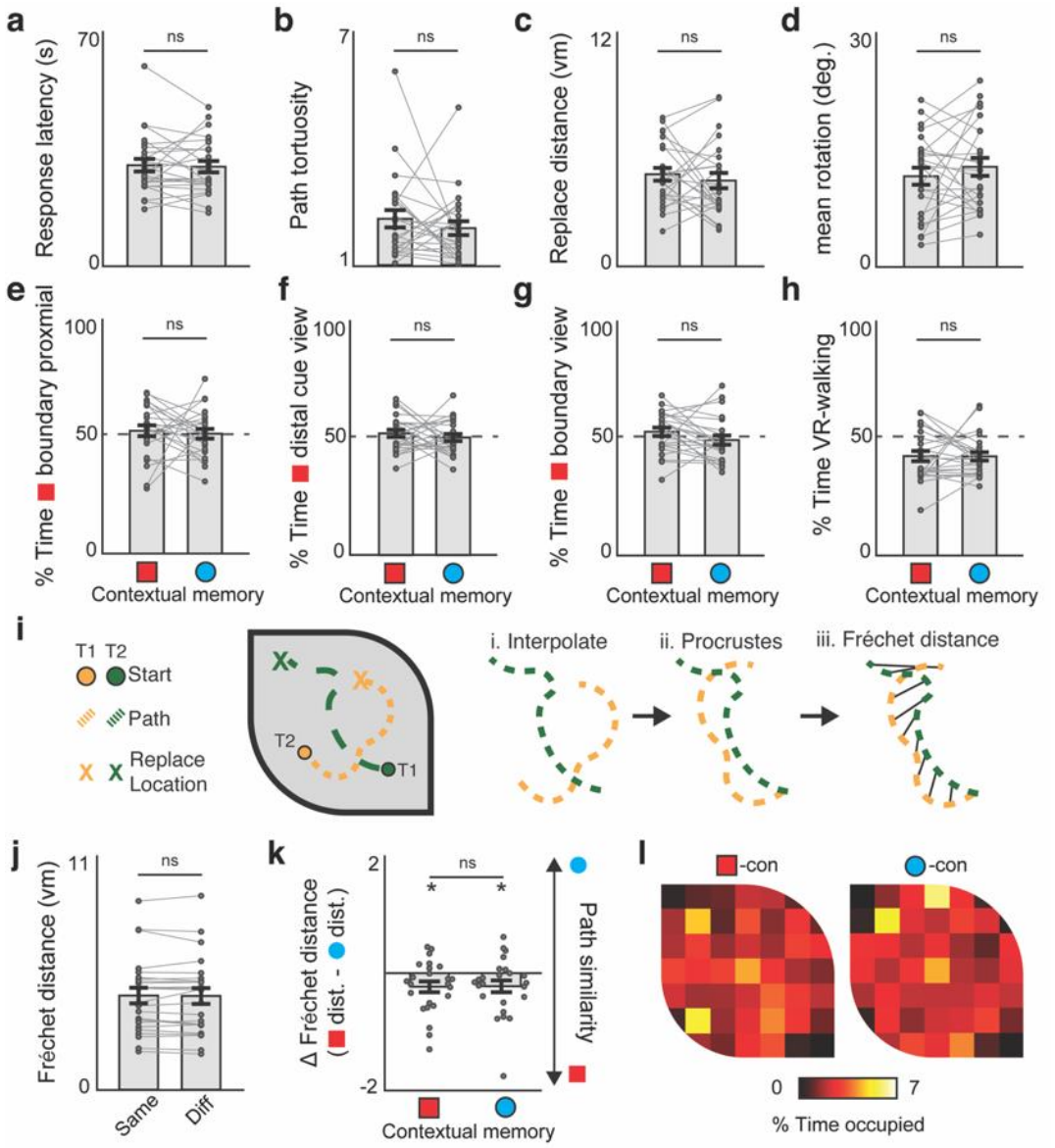

Extended Data Figure 2. No systematic behavioral differences between Square- and Circle-consistent Squircle trials. a-h, Comparison of behavioral measures between Square-consistent (Sq-con) and Circle-consistent (Ci-con) Squircle trials: **a,** response latency (Sq-con vs Ci-con: t_{23}=0.30, p=0.767), **b,** path tortuosity (t_{23}=0.87, p=0.393), **c,** distance of replaced objects from the context-consistent location (t_{23}=0.76, p=0.456), **d,** mean absolute angular difference in allocentric VR-facing direction between successive fMRI volumes, which reflects tendency to rotate VR-heading (t_{23}=1.01, p=0.325), **e,** percentage (%) of time spent in locations proximal to Sq (vs. Ci) boundary segments (t_{23}=0.697, p=0.394), **f,** % time viewing distal cues present in the Sq (vs. Ci) (t_{23}=0.77, p=0.448), **g,** % time spent viewing square (vs. circular) boundary segments (t_{23}=1.58, p=0.127), and **h,** % time spent VR-walking (vs. VR-stationary) (t_{23}=0.06, p=0.956). **i,** Comparison between the shapes of Squircle VR-walking path trajectories across trials. For each pair of trajectories (T1 and T2), i) T2 was interpolated to have the same number of samples as T1 using a spline fit, ii) a Procrustes transformation maximally aligned T1 to T2, and iii) the distance between T1 and T2 was computed using a Fréchet distance metric (see Methods). **j,** The shape of VR-walking path trajectories did not reliably differ between Sq- and Ci-con Squircle trials: the average Frèchet distance between trajectories from trials sharing the same contextual memory (Same) did not differ from those with different contextual memories (Diff) (t_{23}=0.39, p=0.704). **k**, The Frèchet distance was computed between each Squircle trajectory and trajectories in the Sq and Ci. The difference between Squircle-Sq minus Squircle-Ci Frèchet distances were then computed, separately for Sq- and Ci-con Squircle trials. Positive (negative) values thus indicate that Squircle trajectories were more like those in the Sq (Ci). Squircle trajectories were more similar in shape to Sq trajectories, during both Sq-con (t_{23}=2.56, p=0.018) and Ci-con (t_{23}=2.24, p=0.035) trials. Critically, trajectory shapes did not differ in their similarity to the Sq or Ci across Sq- and Ci-con Squircle trials (t_{23}=0.12, p=0.902). **l,** Percentage of time occupying different locations in the Squircle during Sq-con (left) and Ci-con (right) trials, averaged across participants. Only 2% (1/49) of local Squircle regions showed differential sampling between Sq- and Ci-con trials (t-test, p<0.05, uncorrected for multiple comparisons). Throughout the figure, error bars indicate ±1 SEM. All t-test two-tailed. Dots denote individual participants (n=24). ^{ns}p>0.05, *p<0.05.

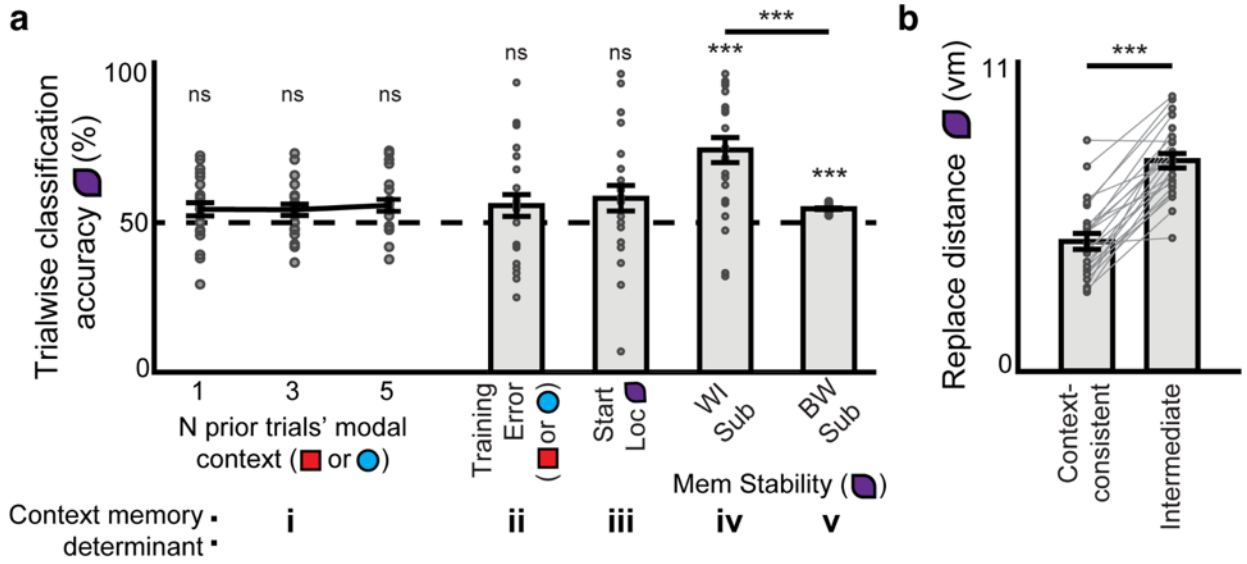

Extended Data Figure 3. Behavioral determinants of Squircle contextual memory retrieval. a, We examined five different possible determinants of trial-by-trial contextual memory retrieval in the Squircle. For each possible determinant, we tested whether that determinant predicted contextual memory retrieval on each Squircle trial (i.e., a Square- or Circle-consistent replace location) and computed classification accuracy across all trials for each participant (% correct, compared to 50% theoretical chance baseline dotted line). The five determinants included: i) The modal Square (Sq) or Circle (Ci) context during the N odd testing trials prior to each individual Squircle trial. Although trial order was balanced across all Squircle trials, for each individual trial, participants were tested more often in either the Sq or Ci every odd number of prior Sq and Ci trials, which may bias contextual memory. For example, for a given Squircle trial, if the three preceding trials were two Sq and one Ci, a participant may be more likely to retrieve a Sq-consistent memory. We thus tested whether Squircle memory retrieval on each individual Squircle trial was predicted by the modal context of the N=1, 3, 5 prior Sq and Ci trials. However, replace locations in the Squircle were not predicted by the previous trials' modal context (t_{23}=0.98, 1.04, 1.75, p_{FWE}=0.508, 0.462, 0.140 for lags 1,3, and 5, respectively). ii) Distance error during training. Although distance error during training was matched on average between the Sq and Ci, for each target object each participant had numerically lower distance error for that object in one of the two training contexts. For each participant, we tested whether Squircle contextual memory was determined by whichever training context had the lowest distance error for each object. Classification accuracy was not significantly higher than expected by chance (t_{23}= 0.985, p=0.335). iii) Squircle trial start location. Each Squircle trial started a random arena location, which may have biased contextual memory. For each Squircle trial, we tested whether contextual memory retrieval was predicted by whichever context-consistent location was nearest to that trial's starting location. Prediction accuracy was not significantly higher than expected by chance (t_{23}=1.41, p=0.175). iv) Contextual memory stability (Mem Stability) across Squircle trials *within* (WI) the same participant. For each target object, did each participant retrieve the same contextual memory for that object across all Squircle trials? For each Squircle trial, we tested whether memory was predicted by the modal contextual memory retrieved on all other Squircle trials for the same target object. We repeated this separately for each participant. For each target object, participants tended to retrieve the same contextual memory for that object across Squircle trials (t_{23}= 5.28, p=2.34x10^{-5}). v) Mem Stability across Squircle trials *between* (BW) participants. For each target object, did each participant retrieve the same contextual memory for that object as the other participants? For each Squircle trial, we tested whether memory was predicted by the modal contextual memory retrieved for that trial's target object by a different participant across all Squircle trials, jackknifed across all participants. For each target object, participants tended to retrieve the same contextual memory as other participants (t_{23}=9.58, 1.70x10^{-9}). However, choice stability was lower across participants than within the same participant (t_{23}=4.73, p=9.22x10^{-5}), indicating that although there was some choice stability between participants, each participant tended to have a unique contextual preference. **b)** Participants replaced target objects in the Squircle closer to a context-consistent location than to the location intermediate between the two context-consistent locations (t=10.86, p=1.57x10^{-10}), and this was the case in 23/24 (96%) individual participants, providing further evidence that participants retrieved either the Square or Circle-consistent contextual memories in the Squircle. Throughout the figure, error bars indicate ±1 SEM; All t-test two-tailed; Dots denote individual participants (n=24). ^{ns}p>0.05, ***p<0.001.

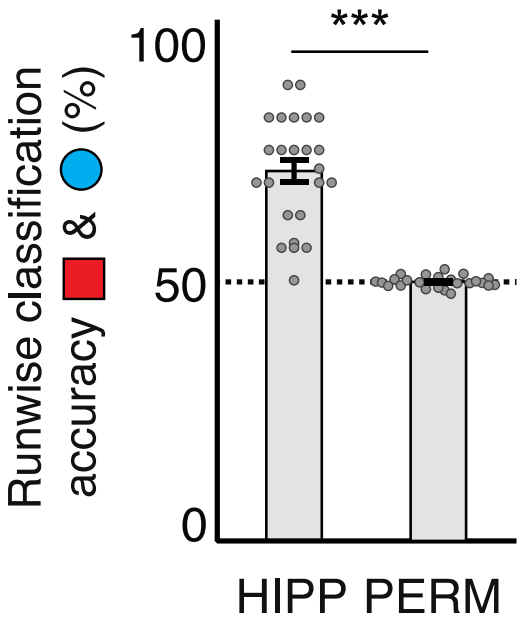

Extended Data Figure 4. Across-run hippocampal Square and Circle context decoding. A single estimate of the average bilateral hippocampal (HIPP) activation pattern for the Square (Sq) and Circle (Ci) was computed for each scan run. Across-run HIPP context classification accuracy for the Sq and Ci was significantly higher than in a permutation test (PERM). The dotted line indicates theoretical chance baseline (50%). Error bars indicate ±1 SEM. Dots denote individual participants (n=24). ***p<0.001.

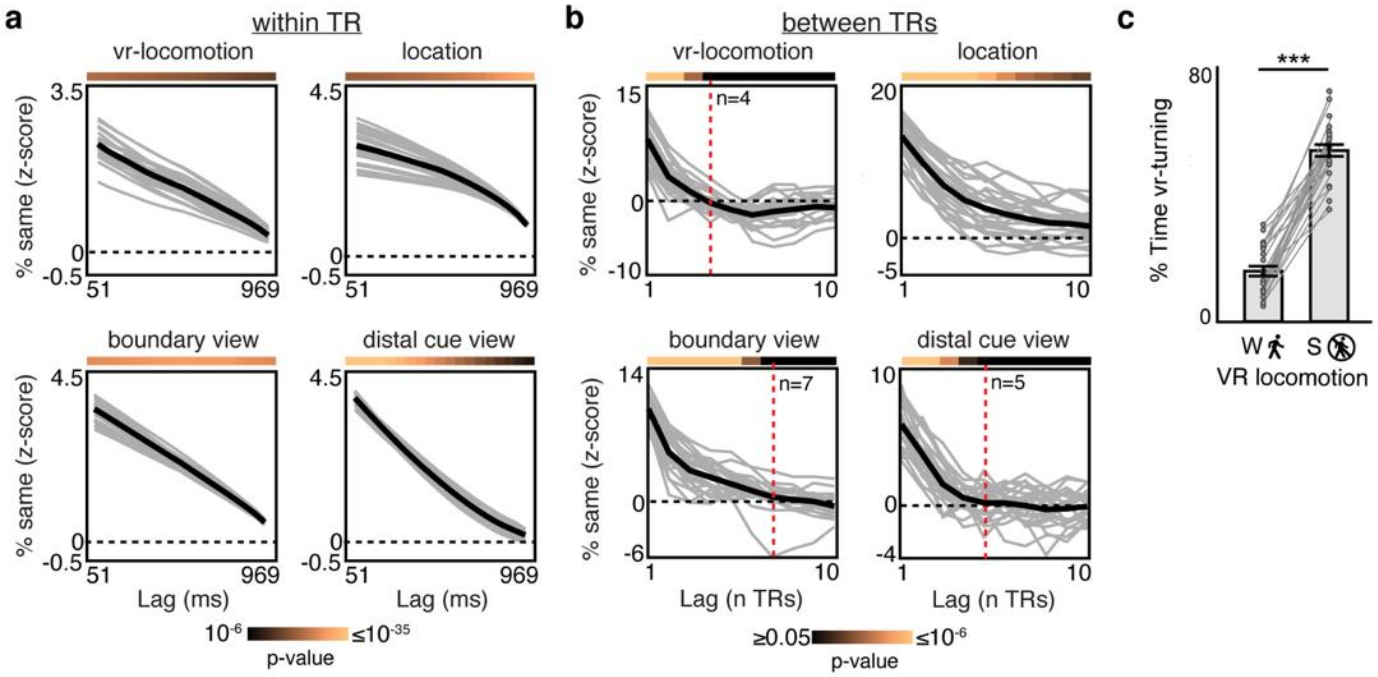

Extended Data Figure 5. Behavioral control analyses in the Squircle. a, To unambiguously compute CS Scores for each nonmnemonic behavioral factor given the fMRI signal's hemodynamic lag, each factor must be temporally autocorrelated during Squircle trials within and across fMRI volumes. To determine the temporal autocorrelation within fMRI volume (TR), we computed the percentage of timepoints during which nonmnemonic factors were the same between timepoint t and t+N, where N corresponds to 19 lags from 51-969 msec from t (i.e., at the behavioral sampling rate—20Hz), within a single TR during Squircle trials. Nonmnemonic factors include VR-locomotion (VR-walking or -stationary), location (most proximal boundary segment, either Square or Circle), boundary view (toward Square or Circle boundary segment), distal cue view (toward Square or Circle distal cue). To control for potential nonuniform sampling within each nonmnemonic factor, percentages were converted to z-scores by randomly shuffling each nonmnemonic factor across timepoints separately for each participant (k=500). Each nonmnemonic factor was more similar across successive timepoints within TRs at all lags than expected by chance (color bars denote p-values from one-sample t-tests compared to 0 baseline; all t_{23}>9.82, $p<10^{-8}$). Light gray lines denote individual participants (n=24), black line denotes group mean. **b,** Same as in **(a)** but between successive TRs (lags 1-10 TRs) during Squircle trials. Red dotted lines denote the lag N at which a given nonmnemonic factor was no more likely to be the same at time t than t+N (t-test, p>0.05, uncorrected for multiple comparisons), if at all. Participants tended to occupy the same behavioral state for multiple TRs. **c,** Percentage of time during Squircle trials that participants VR-turned (mean angular velocity >0 deg/sec) between successive TRs during VR-walking and -stationary epochs. Participants VR-turned more often during VR-stationary than -walking epochs (t_{23}=17.28, $p=1.13\times10^{-14}$). This result also implies that both boundary view and distal cue view were more similar across successive TRs during VR-walking than VR-stationary epochs. Error bars indicate ±1 SEM. Dots denote individual participants (n=24). Throughout the figure, all t-tests two-tailed. ***p<0.001.

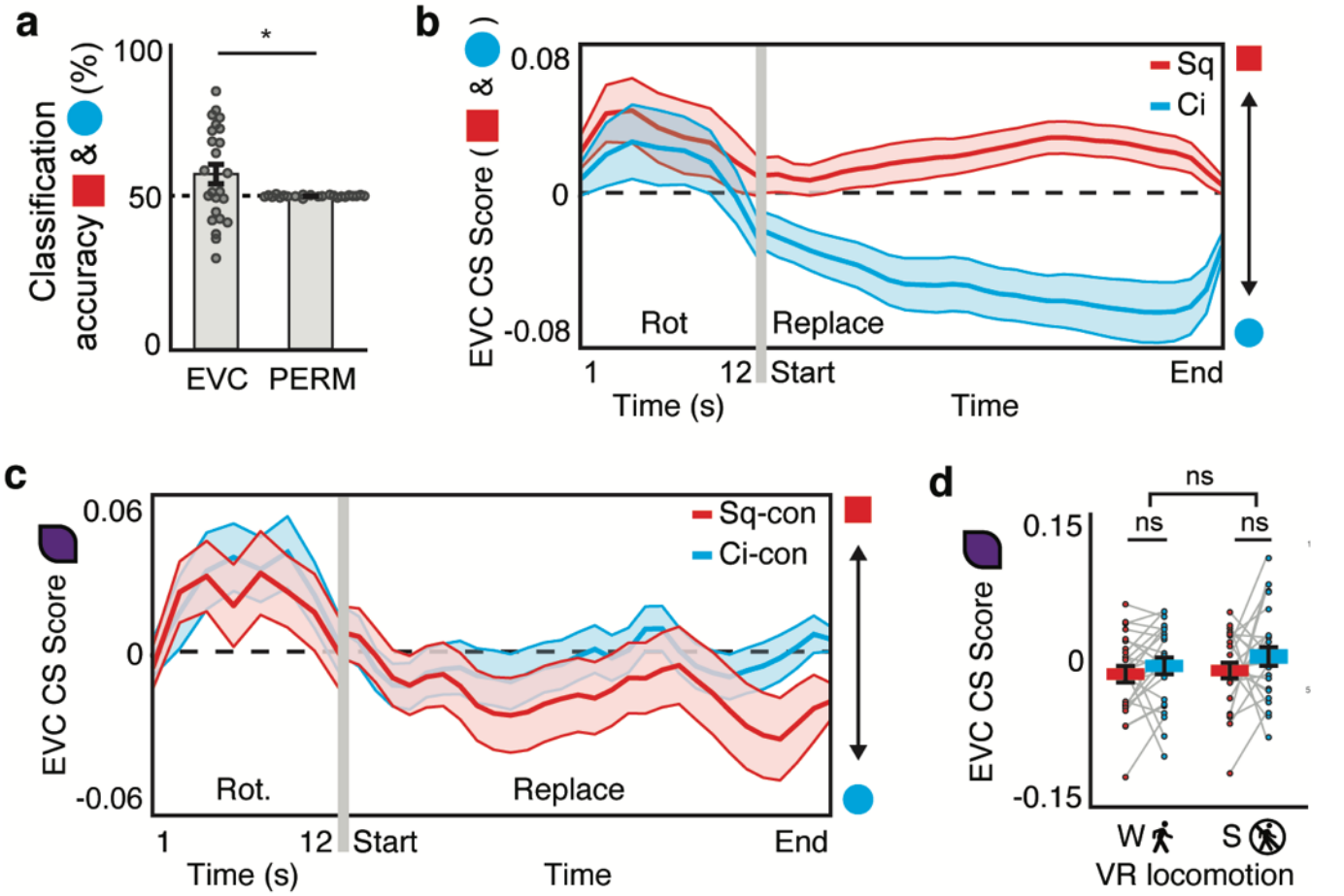

Extended Data Figure 6. Early visual cortex context decoding. a, Leave-one-run-out cross-validated trial-by-trial context classification accuracy from the EVC was higher than chance (57.1% versus 49.9% in the permutation test, t_{23}=2.31, p=0.015; t_{23}=2.24, p=0.018 compared to 50% theoretical chance baseline). Though fewer participants had numerically greater context classification accuracy than expected in the permutation test in EVC than the hippocampus (n=24, McNemar X^2 test with Yates' correction, X^2=4.03, p=0.045, two-tailed), this result nonetheless indicates that there tended to be different EVC activation patterns elicited in the Square and Circle, as expected given that the two contexts were visually distinct. **b,** Contextual similarity of EVC activity over time during Sq (red) and Ci (blue) trials. **c,** EVC CS Scores over time during Sq-con and Ci-con Squircle trials (Sq-con vs Ci-con replace phase: t_{23}=-1.63, p=0.942, t-test, one-tailed). **d**, EVC Sq-con and Ci-con Squircle CS Scores binned by VR-locomotory behavior (contextual memory x VR-locomotion rmANOVA: VR-locomotion main effect, $F_{1,23}$=1.69, p=0.207; interaction, $F_{1,23}$=0.25, p=0.624). Throughout the figure, error bars or error bands indicate ±1 SEM. Dots denote individual participants (n=24). Post-hoc t-tests were 1-tailed. ^{ns}p>0.05, *p<0.05, **p<0.01, ***p<0.001.

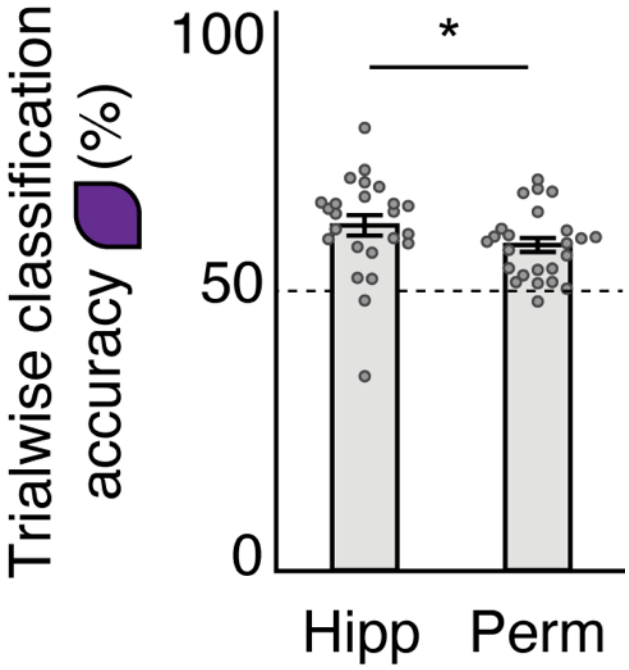

Extended Data Figure 7. Target-object-invariant CS Scores in the Squircle. Trial-by-trial hippocampal Squircle contextual memory classification accuracy from the target-object-invariant context classifier, using data from VR-walking epochs, was significantly higher than expected by chance (61.6% versus 58.0% in the permutation test, t_{23}=1.98, p=0.030; t_{23}=6.34, p=9.0x10^{-7} compared to 50% theoretical chance baseline). Thus, hippocampal context representations during VR-walking epochs were tolerant to changes in target object. Error bars indicate ±1 SEM; Dots denote individual participants (n=24). *p<0.05.

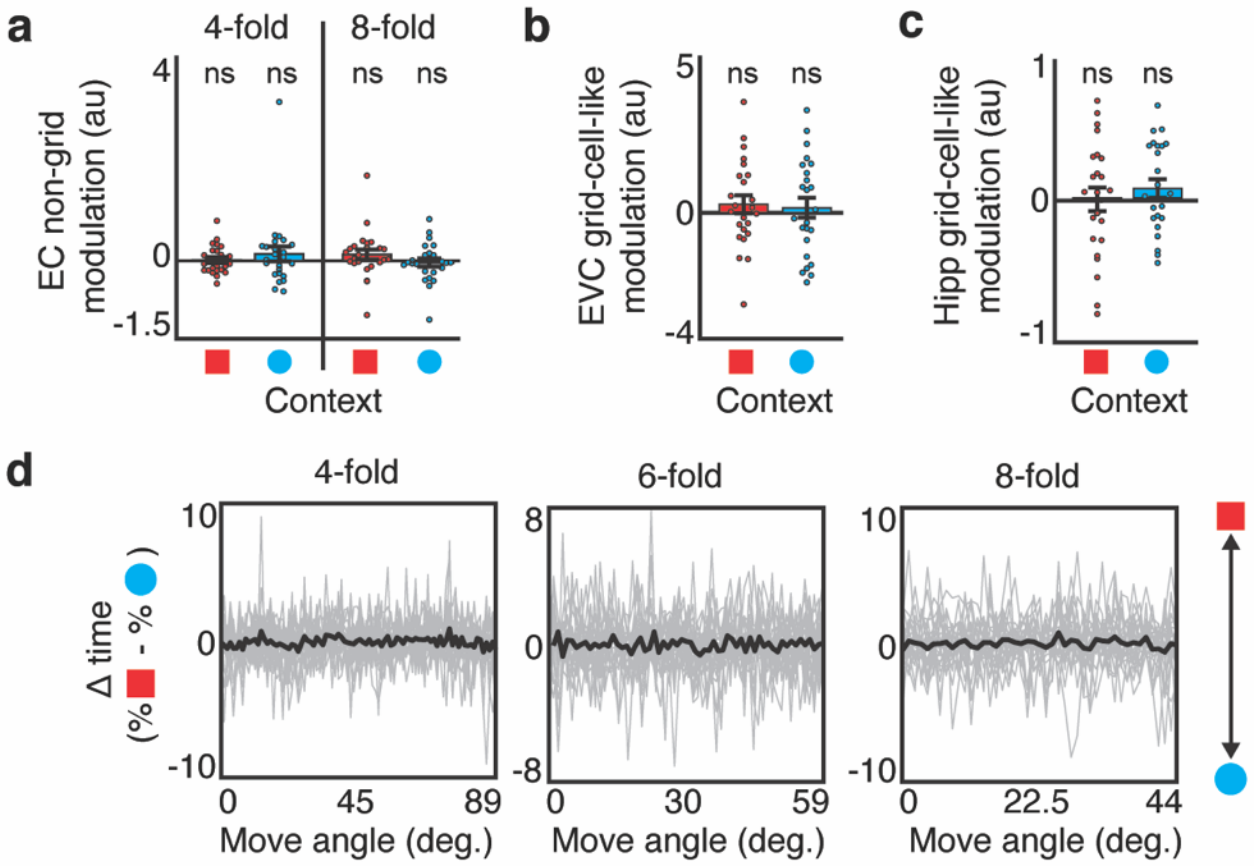

Extended Data Figure 8. Entorhinal grid-like realignment control analyses. a, The strength of reliable periodic modulation (beta weight) as a function of VR-walking direction in the entorhinal (EC) subregion of interest from Figure 4A for 90° (4-fold) and 45° (8-fold) periodicities. These control periodicities were tested in particular because a recent study using human intracranial recordings found a large proportion of EC neurons had spatially periodic firing fields with 90° or 45° rotational symmetry[23]. Neither 90° nor 45° showed significant reliable periodic modulation aligned to their respective orientations in either the Square (Sq) or Circle (Ci) (90°: Sq, t-test t_{23}=0.28, p=0.779, sign-test p=0.541; Ci, t test, t_{23}=0.94, p=0.359, sign-test p=0.839; 45°: Sq, t-test t_{23}=1.26, p=0.110, sign-test p=0.308; Ci, t_{23}=-0.419, p=0.661). Note that these null effects were not specific to the entorhinal subregion based on the 60° periodicity analysis, as we saw no effect for 90° or 45° in any voxels in the entire entorhinal cortex at p_{SVC}<0.05. **b,** The strength of grid-like modulation in the early visual cortex (EVC) region of interest. There was no significant reliable grid-like modulation in EVC in either the Sq (t_{23}=0.94, p=0.180) or Ci (t_{23}=0.498, p=0.312). These null effects were not due to averaging over all voxels in EVC, as there was also no grid-like modulation observed in the entire EVC at p_{SVC}<0.05. **c,** The strength of grid-like modulation in the hippocampus (Hipp) region of interest. There was no significant reliable grid-like modulation in Hipp in either the Sq (t_{23}=0.12, p=0.454) or Ci (t_{23}=1.01, p=0.161). These null effects were not due to averaging over all voxels in Hipp, as there was also no grid-like modulation observed in the entire Hipp ROI at p_{SVC}<0.05. **d,** Difference in the percentage of VR-walking directions modulo 90°, 60°, and 45° across the Sq and Ci. To align VR-walking directions across the Sq and Ci, for each periodicity (90°, 60°, and 45°), 0° corresponds to the orientation that maximized entorhinal periodic modulation for that periodicity, separately for the Sq and Ci. Black lines denote means across all participants, and grey lines denote individual participants. There were no differences in periodic VR-walking direction bias (t-test against zero, α=0.05, FWE-corrected) between the Sq and Ci that would be confounded with the presence of context-specific 60° periodic fMRI signal dependent on VR-walking direction Throughout the figure, error bars indicate ±1 SEM. Dots denote individual participants (n=24). ^{ns}p>0.05.

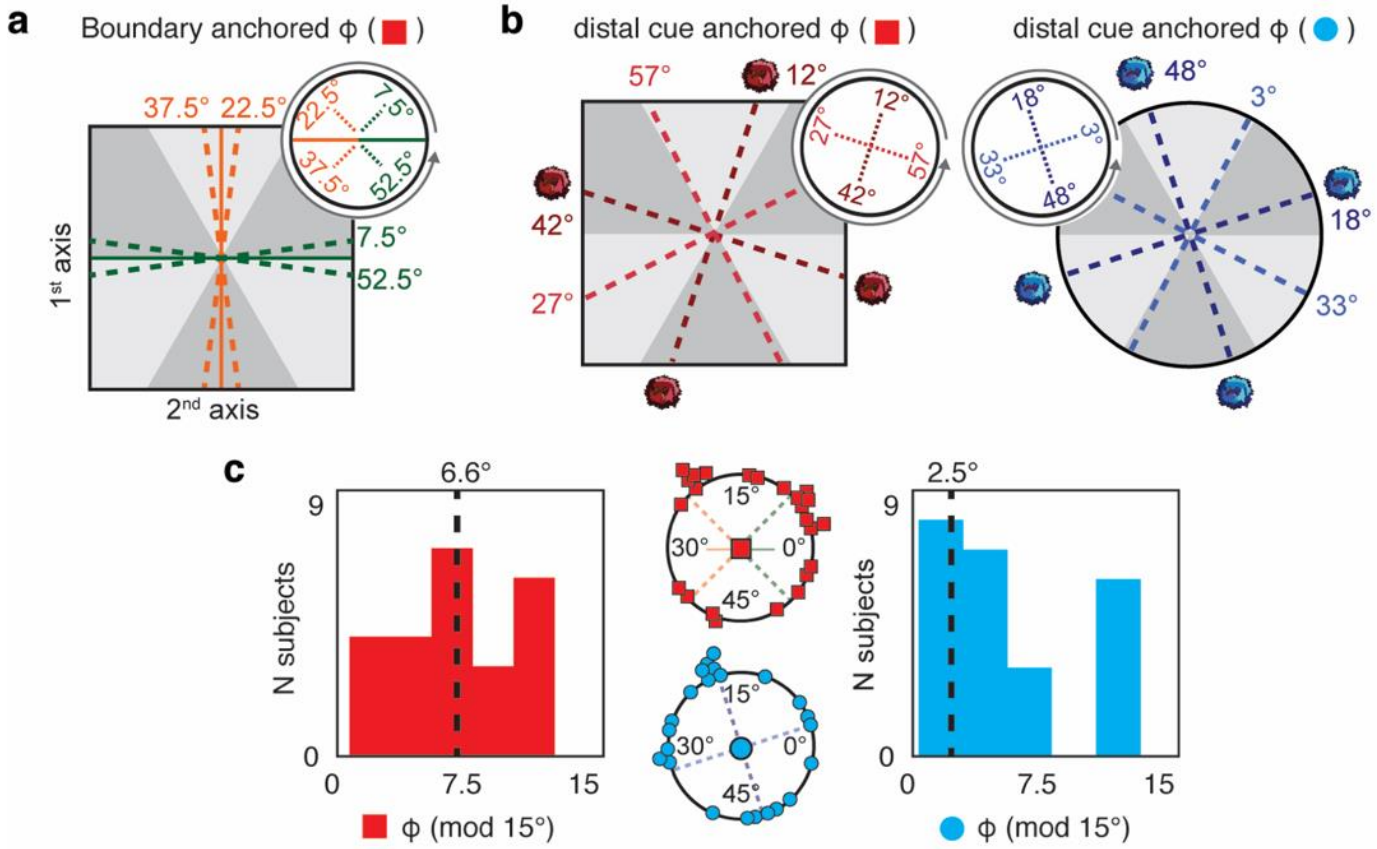

Extended Data Figure 9. Local environmental anchoring of entorhinal grid-like orientations in the Square and Circle. a, Grid orientations (φ) can only be compared across contexts relative to some common reference frame. Here, we used the Squircle as the common reference frame; however, this reference frame choice may have been arbitrary, particularly because participants were not exposed to the Squircle until after having already learned the location-context associations in the Square and Circle. To provide further evidence for grid realignment, we therefore tested whether φs were differentially aligned to local orientational cues in the Square and Circle. In square environments, φ has been found to be offset 7.5° from the boundaries[26,27]. Since φ ranges between 0°-60°, we tested whether Sq φ clustered around four possible angles, each 7.5° from one of the two cardinal axes of the square boundaries. To do so, we folded the grid orientations of all participants by φ mod 15°, which would align all hypothesis-consistent alignments to 7.5° in a circular 0° to 15° space. **b,** We also tested whether φ was reliably aligned to the Sq or Ci distal cues, either directly (0° offset from a distal cue) or maximally offset between distal cues (45° offset from a distal cue, since distal cues were offset from each other by 90° in each context). In addition to 0° offset, a 45° offset was tested because a prior report suggests that in sparse circular VR-environments with only distal orienting cues, φ is maximally offset from the cues (rather than aligned) (Schroeder, T. N. *et al.* (2018) Entorhinal cortex minimises uncertainty for optimal behaviour. *BioRxiv* 166306). Since φ ranges between 0°-60°, we thus tested whether φ clustered around four possible angles in each context. To do so, we folded the grid orientations of all participants by φ mod 15°, which would align all hypothesis-consistent alignments to 12° in the Sq and 3° in the Circle, in a circular 0° to 15° space. **c,** Boundary and distal cue φ alignment. Middle: average φ in each participant (n=24) in the Sq (red squares, top) and Ci (blue circles, bottom). Left and right: histograms of average φ across participants, modulo 15°. In the Sq (left), φ clustered around 7.5° (V-test, V=5.96, p=0.043), consistent with alignment to the square boundaries, but not around 12° (V=-4.077, p=0.880) which would have been consistent with alignment to the distal cues. In the Ci (right), φ clustered around 3° (V=8.63, p=0.006), consistent with reliable distal cue alignment. Since grid orientations aligned to different local cues in each context, this provides further support for the existence of grid-like realignment between the two training contexts.

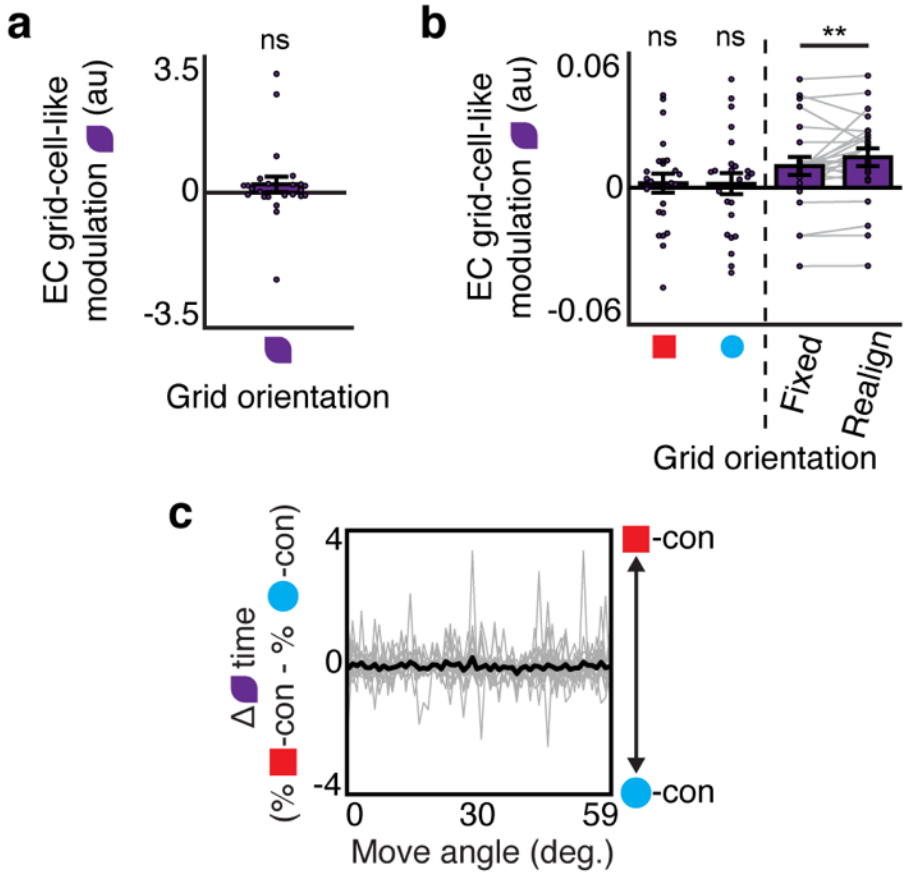

Extended Data Figure 10. Entorhinal grid-like modulation in the ambiguous Squircle context control analyses. a, Grid-like modulation (beta weight) in entorhinal cortex (EC), averaged over all EC voxels, aligned to a single Squircle-specific grid orientation (φ) across all Squircle trials independent of contextual memory. To compute the Squircle-specific φ we performed the same split-half analysis as for the Square (Sq) and Circle (Ci) contexts (e.g., Figure 6), but limited the analysis only to Squircle trials. No significant grid-like modulation (beta weight) was observed when we assumed there was a single Squircle-specific φ (t_{23}=1.06, p=0.149; sign-test p=0.271, one-tailed). **b,** Left: Grid-like modulation in EC, averaged over all EC voxels, aligned to either the Sq φ or the Ci φ across all Squircle trials. No significant grid-like modulation was observed (Sq, t- test t_{23}=0.50, p=0.312; Ci, t test, t_{23}=0.39, p=0.350). Right: An alternative possibility is that EC grid representations have a single fixed φ (either Sq φ or Ci φ) across all Squircle trials, but whether the Squircle φ was the Sq or Ci φ differed across participants. To address this alternative, for each participant, we computed the maximum grid-like modulation observed by a single fixed φ (either the Sq φ or Ci φ, whichever yielded stronger grid-like modulation). We then compared the strength of grid-like modulation aligned to this fixed φ to the maximum grid-like modulation observed if φ realigned across trials (Realign; Figure 6b), independent of contextual memory. Stronger grid-like modulation was observed in the Squircle in the majority of participants (75%; 19/24) if φ realigned on a trial-by-trial basis than if we assumed that there was a fixed φ across all Squircle trials (sign-test, p=0.005, one-tailed; t-test t_{23}=1.92, p=0.034). **c,** Difference in the percentage of VR-walking directions modulo 60° between Sq- and Ci-consistent Squircle trials. There was no difference in periodic VR-walking direction bias between Sq- and Ci-consistent trials that would be confounded with the presence of contextual-memory-specific 60° periodic fMRI signals dependent on VR-walking direction. Throughout the figure, error bars indicate ±1 SEM. Dots denote individual participants (n=24). **p<0.01, ^{ns}p>0.05.

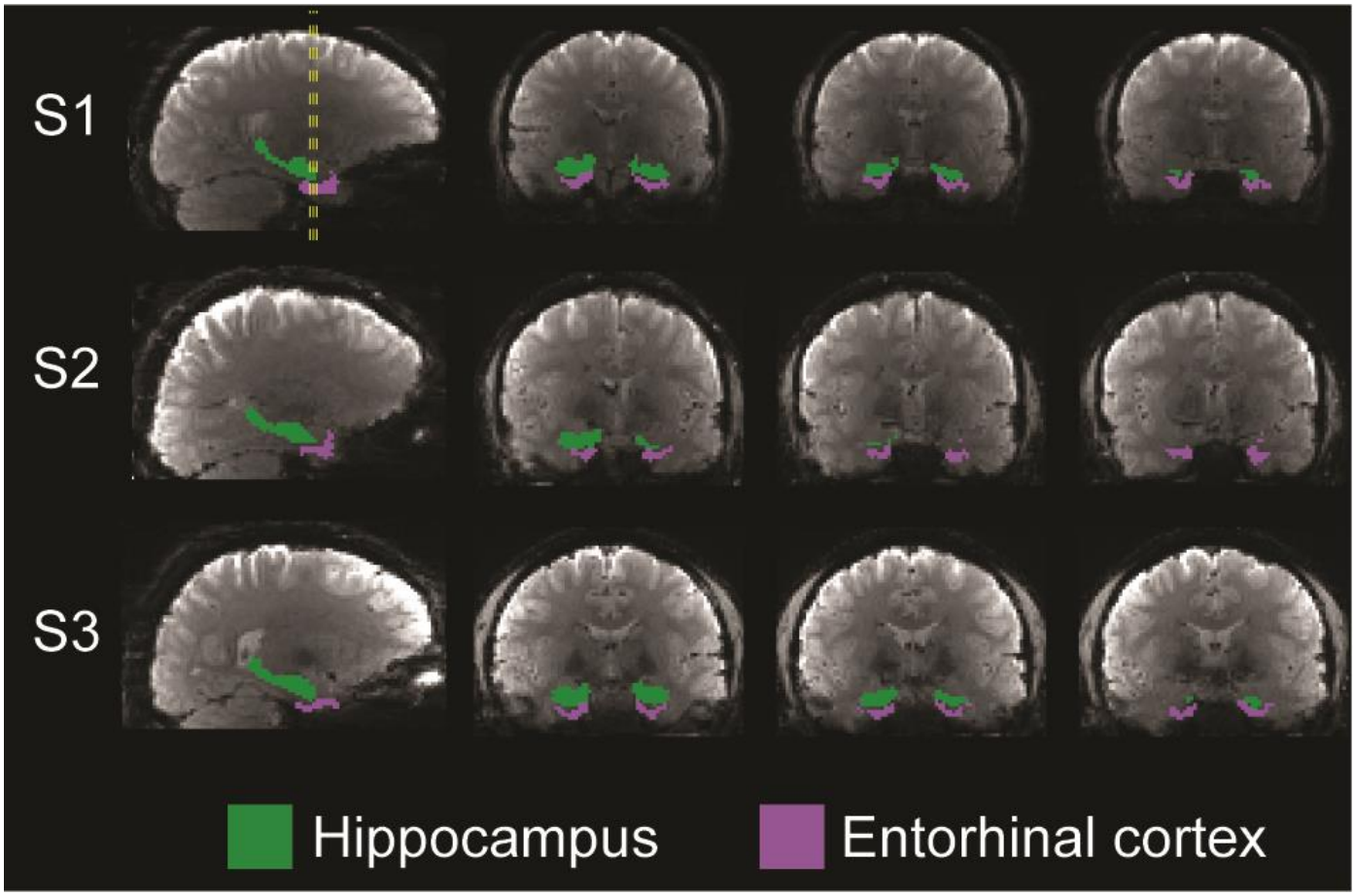

Supplementary Figure 1.

Hippocampal and entorhinal regions of interest. Regions of interest for three representative participants shown overlaid on functional data.

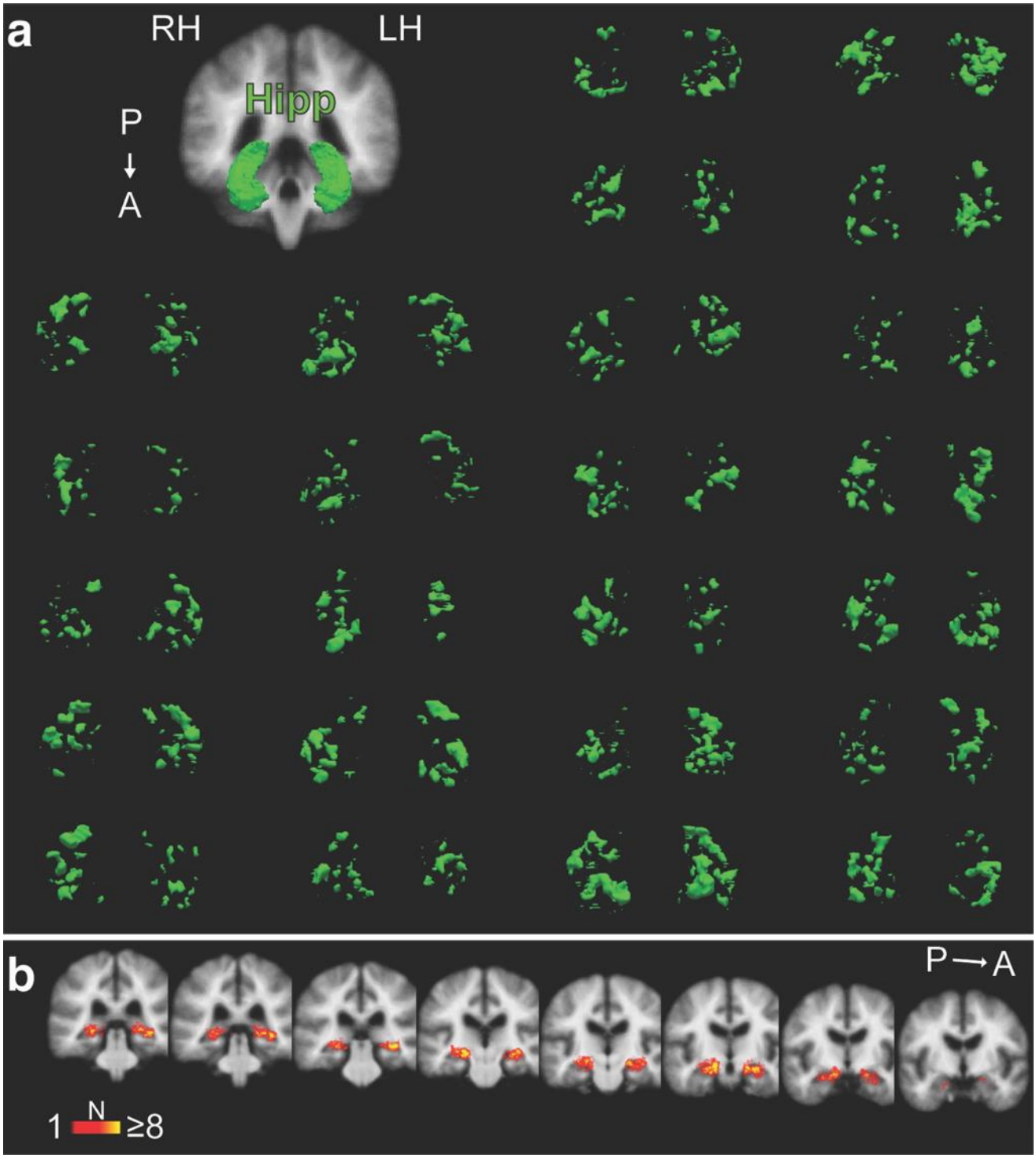

Supplementary Figure 2.

Voxel-selected hippocampal masks.

a, Isosurface of voxel-selected hippocampal mask in each participant (n=24). Masks were constructed for each participant as the union of masks across scan (mean number of 1 mm^3 isotropic voxels per mask per participant: 1120.9; median across participants: 1034; range across participants: 633-2484; standard deviation across participants: 420.3).

b, Voxel-wise overlap of voxel-selected hippocampal masks across all participants. Across participants, voxel-selected hippocampal masks spanned the hippocampal extent.

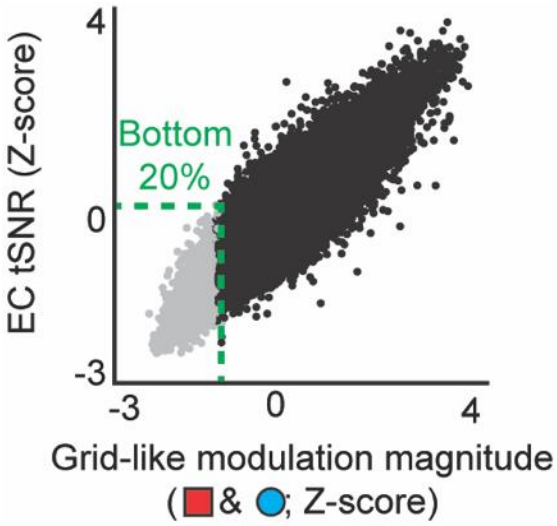

Supplementary Figure 3.

Voxel-wise entorhinal grid-like response magnitude and entorhinal fMRI signal quality.

Comparison of grid-like the response magnitude during Square and Circle trials, averaged across all scan runs and both contexts, and temporal signal to noise ratio (tSNR) across all voxels in entorhinal cortex (EC). Each dot denotes a single EC voxel from a single participant; gray dots denote those voxels with a relatively low grid-like signal and tSNR that were excluded from grid orientation calculations. Both response magnitude and tSNR were *Z*-scored within participant.